Modeling Left Ventricle Wall Motion Using Tagged Magnetic Resonance Imaging

By
Mohammed D. Alenezy

Submitted to the Department of Physics and Astronomy and the Faculty of the Graduate School of the University of Kansas in partial fulfillment of the requirements for the degree of Doctor of Philosophy

Jack J. Shi (Co-chair)

Mehmet Bilgen (Co-Chair)

Chris Fischer

Larry T. Cook

Irina V. Smirnova

March 24, 2009

Date defended

The Dissertation Committee for Mohammed D. Alenezy certifies that this is the approved version of the following dissertation

Modeling Left Ventricle Wall Motion Using Tagged Magnetic Resonance Imaging

Committee:

Jack J. Shi (Co-chair)

Mehmet Bilgen (Co-Chair)

Chris Fischer

Larry T. Cook

Irina V. Smirnova

Date Approved :

Abstract

A two-parameter computational model is proposed for the study of the regional motion of the left ventricle (LV) wall using tagged magnetic resonance imaging (tMRI) data. In this model, the LV wall motion is mathematically decomposed into two components, an isotropic deformation of the LV wall tissues along the short axis of LV and a non-uniform rotation of the tissues along the long axis of LV. The deformation and rotation parameters are determined by fitting the model to tMRI images of the short-axis planes of the LV wall. To validate this model, the tMRI images of the LV wall at the midventricular, apical and basal levels from eight subjects including healthy human, healthy and diabetic rats were studied. The result showed that this model is very effective in studying the LV wall motion and function in both small animals and human. With this model, the torsion, strain, and strain rate of the LV wall tissues can easily be calculated analytically at different phases of a cardiac cycle. It was found that the ratio of the torsion at endocardium to the torsion at epicardium is a constant during the cardiac motion even though the torsion varies with time significantly. The value of this constant of motion equals the ratio of the end diastolic radii of the LV wall at endocardium and epicardium and, therefore, is approximately the same for rats and human.

This dissertation also includes a study of effects of exercise training on diabetic heart. In that study, global cardiac functions were measured using high field MRI and it was found that the global functions of diabetic heart could be improved by the training.

Table of Contents

List of Figures

List of Tables

Chapter 1 : Introduction

Heart disease is the leading cause of death worldwide. Many diagnostic techniques have been developed to understand and treat cardiovascular diseases. Cardiac imaging is one of the important methods that have been widely utilized for diagnosing heart and vascular diseases in clinical practices. It provides physicians with valuable information that can be used to monitor cardiac function and determine the right treatment. Figure 1.1 illustrates a cross-section of a human heart. From the long axis view (the vertical direction in Fig. 1.1), the upper portion of the heart is, clinically, known as the base, the lower portion is the apex, and the middle portion is the midventricle. Heart wall can be divided from short axis view (the horizontal direction in Fig. 1.1) into three layers, namely: epicardium, midcardium, and endocardium, ordered from outer to inner layer. The heart consists of four main chambers, left atrium (LA), right atrium (RA), left ventricle (LV), and right ventricle (RV). Being the largest and the strongest chamber of the heart, LV has thicker wall and it is responsible for pumping the oxygenated and purified blood to the whole body. Left Ventricle has been the target of many studies on the evaluation of heart performance.

In the diagnosis of heart diseases, global functions such as stroke volume and ejection fraction are important parameters for evaluating heart performance. For some heart dysfunction, however, a study of the global functions alone cannot detect regional abnormalities of cardiac tissues. Instead, regional cardiac functions need to be evaluated through a detailed information of heart wall motion. While qualitative

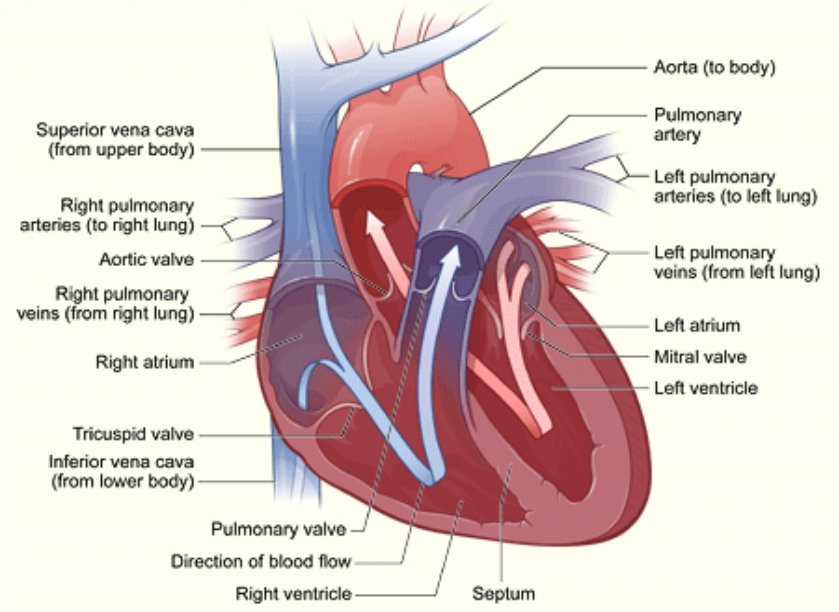

Figure 1.1: Cross-section of a human heart. The arrow pointing to the upright indicates the direction of the oxygen-poor blood flowing from the body to the lungs and the arrow pointing to the upleft shows the direction of the oxygen-rich blood flowing from the lungs to the body.

heart wall motion analysis has proven valuable in clinical cardiology practice, quantitative modeling of the heart wall motion is more important but remains a challenge task because of the complicated structure of the cardiac tissues.

Over the past few years, many works have been published on the study of the left ventricle (LV) wall motion using various computational and mathematical approaches [1]. Among them, the finite element method has been a popular computational tool. To model the heart wall function with the finite element method, it requires a knowledge of the material (mechanical) property and boundary condition of the heart wall tissues [2]. The mechanical properties of a tissue could be estimated by fitting the data from clinical images while the boundary condition has to be assumed or simulated. The accuracy of the modeling with the finite element method

is therefore limited by the accuracy of the boundary condition and the fitted mechanical properties. For a complicated boundary condition or complicated mechanical properties, the finite element modeling is also computationally time-consuming. With a unique ability to create traceable markers non invasively, tagged magnetic resonance imaging (tMRI) opens a new window to study the cardiac motion by making it possible to follow the regional changes of heart tissue during cardiac cycles without any surgical intervention. In tMRI, a mesh of magnetization tag lines are created on a tissue by a pulse of spatially modulated magnetic field (SPAMM). As the tag lines are magnetically attached on a tissue and visible on MRI images, the motion of the tissue can be studied by tracking the motion of the tag lines. Many studies have been conducted to examine the heart functions by directly tracking the tag lines using tMRI data [3-6]. The accuracy and efficiency of those direct methods are, however, limited by the resolution of tMRI images. To study the heart wall motion with directly tracking the tags lines, moreover, one needs a fairly large number of tMRI images in a cardiac cycle. The harmonic phase analysis of tMRI (HARP) is another commonly used method for studying cardiac motion with tMRI data [7]. With HARP, motion of a point on the tag lines is tracked by its constant harmonic phase during the cardiac motion and the mechanical strain of the tissue can also be estimated through the gradient of the harmonic phase. The efficiency of HARP is, however, limited by the wrapping effect, i.e. there could be more than one point on the tag lines that have the same harmonic phase because of the periodicity of the tagging. To prevent the wrapping effect, the deformation between two successive

MRI images has to be small and, therefore, there must be enough number of MRI images to cover a cardiac cycle.

Recently, Alrefae *et al*. introduced a computational model that uses a Gaussian-type function to describe the heart wall deformation at the midventricle of LV where the twist motion of the LV wall is negligible [8]. In that model, the deformation function is fitted to the magnetization tag lines of tMRI images. As a closed-form of the inverse of this Gaussian-type deformation function is not available, the fitting procedure in that model is computationally complicated and inefficient. To overcome this problem, in this dissertation, we propose a new deformation function that is inversely proportional to the square of the distance to the center of LV with a proportional coefficient measuring the severity of the deformation. This new deformation function was also found to be a better function in approximating the LV wall deformation during a cardiac cycle. To study the cardiac motion where the twist motion is important, we model the LV wall motion in the short axis plane as a superposition of the deformation along the short axis of LV and a rotation along the long axis of LV. The rotation of the LV wall is approximated by a two-dimensional rotational transformation with the rotational angle being inversely proportional to the distance to the center of LV. To validate our model, the LV wall motion of eight subjects including two healthy humans, five healthy and one diabetic rats were studied by comparing the model calculation with the tMRI data obtained from the midventricle, apex and base of LV. The study showed that this two parameter model is effective in describing the LV wall motion. One advantage of

using this model to study the LV wall motion is that the torsion and strain of the LV wall tissues can be easily calculated analytically at different phases of a cardiac cycle. A new phenomenon discovered with this model is a constant associates with the LV wall motion. It was found that the ratio of the torsion at endocardium to the torsion at epicardium is a constant during the cardiac motion. The value of this constant of motion equals the ratio of the end diastolic radii of the LV wall at endocardium and epicardium and, therefore, it is quite similar for rats and human. Considering that the torsion varies with time significantly during a cardiac cycle and rat and human have very different values of torsion, this constant of the cardiac motion is quite significant.

In this dissertation, the global cardiac functions were also studied by using high field MRI (9.4 T) . The Cine MRI images of full cardiac cycle were used to calculate the end systolic volume, the end diastolic volume, the stroke volume, and the ejection fraction of diabetic and healthy rat hearts. It was found that the LV dysfunctions of diabetic rat hearts could be detected by assessing those global cardiac functions with high field MRI. The effect of exercises on the diabetic heart functions was also studied with a group of exercised diabetic rats. The study of the global cardiac functions showed that the cardiac performance of diabetic hearts was significantly improved by exercises. Moreover, the volume-time profile of the exercised diabetic hearts was found to be very similar to that of a healthy heart, which further shows the importance of exercise on the improvement of cardiac functions of a diabetic heart.

This dissertation is organized as follows: Chapter 2 is a brief description of the physics of MRI and tagged MRI. The modeling of the LV wall motion is presented in Chapter 3. Chapter 4 contains a study of the global functions of diabetic and healthy hearts using high field MRI.

Chapter 2 : A brief Introduction of Magnetic Resonance Imaging

2.1 Principle of MRI

Biological tissues contain about 63% of their body as hydrogen. Since hydrogen has a nonzero magnetic moment in its nucleus due to the spin of proton, one can obtain a profile of the hydrogen concentration of the tissue that in turn provides physical and biological information of the tissue by using the nuclear magnetic resonance (NMR) technique. This biological and medical application of NMR is referred to Magnetic Resonance Imaging (MRI). Polarization, excitation, and relaxation of magnetic moments of protons are the three main processes of MRI.

2.1.1 Polarization

The magnetic moment of proton is related to its spin $\vec{S}$ as $\vec{\mu} = \gamma\vec{S}$, where γ is the gyromagnetic ratio and equals to 0.268 GHz/T for proton. In the presence of an external magnetic field $\vec{B}_0$, proton spin has two quantum states, $S_+ = \hbar/2$ and $S_- = -\hbar/2$, and the spin energy is $E_\pm = \pm\gamma\hbar B_0/2$, where + and – correspond to the anti-parallel and parallel states, respectively. Consider an ensemble of spins of hydrogen nuclei inside a biological sample. Without external magnetic field, the magnetic moments of the spins are randomly oriented and they cancel each other. Consequently, the net magnetic moment (magnetization) of the sample is zero. With an external magnetic field, the magnetization of the sample is

$$M = (n_+ - n_-)\,\mu = \frac{\hbar\gamma}{2}(n_+ - n_-) \qquad (2.1)$$

where n_+ and $n\_$ are the number of spins parallel and anti-parallel to the $\vec{B}_0$ field, respectively. Based on the Boltzmann distribution,

$$n_+ = N\frac{e^{-\frac{E_+}{kT}}}{e^{-\frac{E_+}{kT}} + e^{-\frac{E_-}{kT}}} \tag{2.2}$$

where $N = n_+ + n_-$ is the total number of the spins. The magnetization of the sample can be calculated as

$$M = \frac{\gamma\hbar N}{2}\tanh(\frac{\gamma\hbar B_0}{2kT}) \tag{2.3}$$

In a biological sample that contains about 1mL of water, there are about 10^{22} hydrogen nuclei, and at the room temperature (T=300K) and $B_0 = 10T$, this number of nuclei will produce magnetization M of about 10^{-9} J/T which is strong enough to be detected by the MRI receiving coil.

The dynamics of the magnetization inside an external field $\vec{B}$ is govern by the Bloch equation,

$$\frac{d\vec{M}}{dt} = \gamma\vec{M} \times \vec{B} \tag{2.4}$$

In the case of a constant magnetic field in the z-direction $\vec{B} = B_0\vec{z}$, the Bloch equation can be easily solved as

$$\vec{M}(t) = \begin{bmatrix} M_x(t) \\ M_y(t) \\ M_z(t) \end{bmatrix} = \begin{vmatrix} \cos(\omega_0 t) & \sin(\omega_0 t) & 0 \\ -\sin(\omega_0 t) & \cos(\omega_0 t) & 0 \\ 0 & 0 & 1 \end{vmatrix} \begin{bmatrix} M_x(0) \\ M_y(0) \\ M_z(0) \end{bmatrix} \tag{2.5}$$

where $\omega_0 = \gamma B_0$ is the Larmor frequency. Applying the initial conditions on the above equation at t=0, the magnetization vectors will be given by:

$$M_x = M_y = 0, \quad M_z = M \tag{2.6}$$

Therefore, $\vec{M}$ is a constant and there is no induced current in the receiving coil. In this case, there is no MRI signal.

2.1.2 Excitation

In order to generate a MRI signal, $\vec{M}$ needs to be perturbed from its original direction given in Eq. (2.6). To perturb M, another pulsed magnetic field $\vec{B}_1$ that is perpendicular to $\vec{B}_0$ and oscillated with a RF frequency is used where B1<<B0. When this RF pulse is turned on, $\vec{M}$ will be shifted from z-axis by an angle β (flip angle of the RF pulse). If the frequency of B1 is the same as the Larmor frequency ω_0, $\vec{M}$ will precess around $\vec{B}_1$. When the RF pulse is off, $\vec{M}$ will rotate around $\vec{B}_0$ after a relaxation time T_2. With $\vec{B}_1$, the magnetic field in the Bloch equation is

$$\vec{B} = \vec{B}_0 + \vec{B}_1(t) \tag{2.7}$$

where $B_x = B_1 \cos \omega t$, $B_y = -B_1 \sin \omega t$, $B_z = B_0$, and ω is the frequency of the B_1 field.. Without relaxation (damping), the general solution of the Bloch equation is

$$M_x(t) = M_x(0) \cos \omega_0 + \frac{\gamma B_1 M_0}{\omega_0 - \omega} \cos \omega_0 t \tag{2.8}$$

$$M_y(t) = -M_x(0) \sin \omega_0 - \frac{\gamma B_1 M_0}{\omega_0 - \omega} \sin \omega_0 t \tag{2.9}$$

and M_z can be obtained by substituting Eqs. (2.8) and (2.9) in Eqs. (2.4). With the relaxation, the general solution of the Bloch equation becomes

$$M_x(t) = \frac{\omega_0 B_1}{\xi^2 + (\omega - \omega_0)^2}[\xi \sin \omega\, t + (\omega - \omega_0)\cos \omega\, t] \tag{2.13}$$

$$M_y(t) = -\frac{\omega_0 B_1}{\xi^2 + (\omega - \omega_0)^2}[\xi \cos \omega\, t + (\omega - \omega_0)\sin \omega\, t] \tag{2.14}$$

where ξ is the damping constant. Now the transverse components of $\vec{M}$ are not zero anymore due to the perturbation of $\vec{B}_1$. This tipping of $\vec{M}$ will produce an induction current in a receiving coil that can be detected as a magnetic resonance (MR) signal. Figure 2.1 is an illustration of the detection of MR signal, where the change of the transverse components $\vec{M}_{xy}$ is significant so that the induction current can be detected.

2.1.3 Relaxation

Bloch equation (equation 2.4) needs to be corrected by adding Relaxation which is related to the energy exchange between spins (T_2 relaxation), and between spins and lattice (T_1 relaxation).

2.1.3.1 T_1 relaxation:

Spin-lattice relaxation is the process that is responsible for the returning of the longitudinal component $\vec{M}_z$ to its original value (Fig. 2.2), this mechanism is represented by the following equation:

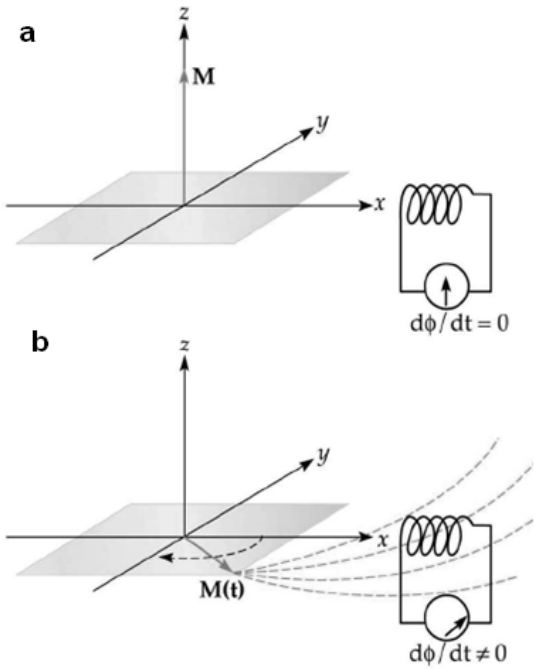

Figure 2.1 : a) $\vec{M}$ is in z-direction, no signal will be detected by the receiving coil; b) $\vec{M}$ is in the xy-plane, the signal can be detected by the receiving coil [9].

$$\frac{d\vec{M}_z}{dt} = -\frac{\vec{M}_z - \vec{M}_0}{T_1} \tag{2.15}$$

This T_1 recovery (relaxation) arises from the nuclear spin interactions with the entire solid or liquid lattice; energy that was absorbed by the spin system from the perturbing RF source is transferred now to the lattice. The differential equation in 1.12 can be easily solved for $\vec{M}_z$ to give

$$\vec{M}_z = \vec{M}_0(1 - e^{-\frac{t}{T_1}}) \tag{2.16}$$

Where $\vec{M}_0$ the equilibrium magnetization and T_1 is is the longitudinal relaxation time.

2.1.3.2 T_2 relaxation:

The second mechanism of the relaxation process is the spin-spin relaxation or T_2 decay which results from the interaction of the nuclear spins with each other, and it is the time needed for all the spins in the xy- plane to cancel each other (Fig 2.3). This process characterizes the $\vec{M}_{xy}$ component; and it can be represented by the following two equations:

$$\frac{d\vec{M}_x}{dt} = \gamma(\vec{M}_y B_0) - \frac{\vec{M}_x}{T_2} \tag{2.17}$$

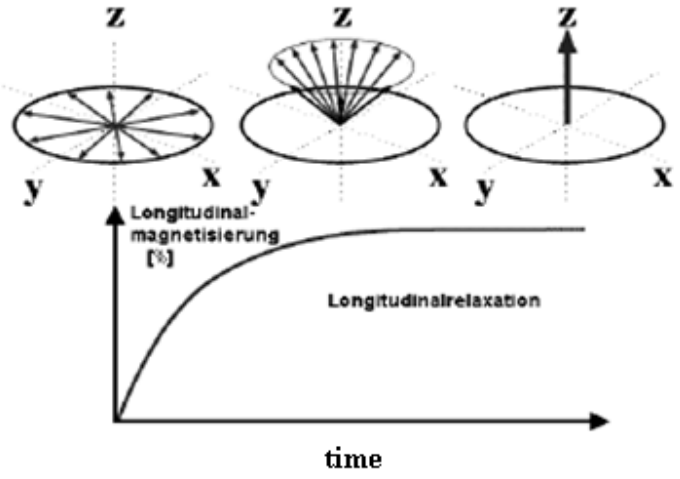

Figure 2.2 : T_1 relaxation process, where $\vec{M}_z$ needs T_1 times to return to about 63% of its original value [9]

$$\frac{d\vec{M}_y}{dt} = -\gamma(\vec{M}_x B_0) - \frac{\vec{M}_y}{T_2} \tag{2.18}$$

T_2 relaxation does not change the energy of the spin system but, rather, increases its disorder, and as a result reducing its ability to produce a coherent signal. The above two differential equations can be solved for transverse component $\vec{M}_{xy}$ as:

$$\vec{M}_{xy} = \vec{M}_0 e^{-\frac{t}{T_2}} \tag{2.19}$$

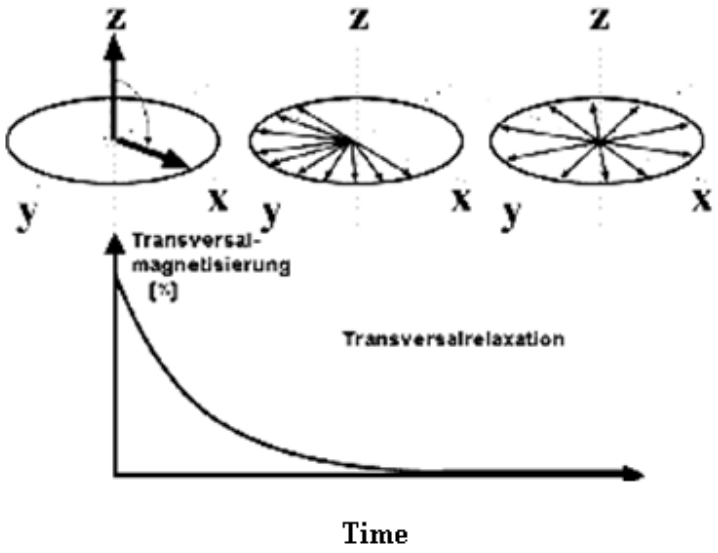

Figure 2.3 : T_2 relaxation process, where M_{xy} needs T_2 times to rephrase (M_{xy}=0) [9].

In general, Bloch equation that can be used to describe the net magnetization motion of the MR signal is given by:

$$\frac{d\vec{M}}{dt} = (\vec{M} \times \gamma\vec{B}) - \frac{M_x\vec{x} + M_y\vec{y}}{T_2} - \frac{(M_z - M_0)\vec{z}}{T_1} \tag{2.20}$$

2.2 Image Contrast

One of the important features of MRI is that you can control the contrast of a certain kind of biological tissue by controlling the repetition time (TR), and the Time of echo (TE) parameters. This is one of the MRI characteristic features over other kinds of imaging techniques. Depending on the kind of tissue that one need to image, the time parameters can be chosen to give a certain contrast to that tissue.

2.2.1 T_1 Weighted Image

TR is defined as the time between two successive RF pulses, and since T_1 is dependent on the kind of the tissue being imaged, then for short TR, the only tissue that will be allowed to recover quickly, before the second RF pulse created, is the tissue with short T_1 (bright); tissues with longer T_1 will be partially recovered and as a result it will have weaker signal (dark). Images with short TR are called T_1 weighted images.

2.2.2 T2 Weighted Image

TE or echo time is defined as the time interval between the RF pulse and the detection of the MR signal. For short T_2, there will be little signal decay (T_2), so the difference between tissues will be small; to get strong T_2 signal, one need longer TE which allows tissues with short T_2 to lose most of their signal and appear dark, where long T_2 tissues still produce strong signal and appear bright. This kind of image is called T_2 weighted image.

2.2.3 Proton Density Image

The third kind of imaging procedure is called proton density, in this procedure, we apply long TR and short TE, to get higher signal to noise ratio, because long TR allows the magnetization vector to recover back to z-axis, where short TE minimize signal decrease due to transverse decay. This kind of images produced in this way is called proton density image. The characteristics of these procedures are summarized in table 2.1.

Table 2.1 :Summary of different image contrast techniques

	Short TR	Long TR
Short TE	T_1- weighted	Proton density (PD)
Long TE	N/A	T_2- weighted

2.3 Cardiac MRI

Providing a noninvasive diagnosis procedure of cardiovascular diseases, Cardiac MRI (CMRI) is considered as promising research field. CMRI technique can provide valuable information on anatomic structure, blood flow velocities, and tissue microstructure This allows this method to assess both physiologic structure and function. Several techniques are being used for Cardiac imaging. Ultrasound, X-ray computed tomography (CT), and MRI are the most common methods that are used for clinical purposes. Echocardiography (Ultrasound) has high temporal resolution and operates conveniently in real-time, but lacks freedom of access to arbitrary imaging planes, is sensitive only to motion in a single direction, and provides decreased soft tissue contrast when compared to MRI. The key advantages of Echocardiography are lower cost, short imaging times, and improved patient comfort,

thus making it a key clinical diagnostics tool. These advantages, however, are outweighed for some applications by the quality of data that can be obtained using MRI. Ultrasound-based techniques are not currently able to characterize regional wall motion estimates spanning the whole heart in a spatio-temporally registered manner. In addition they cannot be sensitized to measure regional myofiber orientation. X-ray computed tomography (CT) is an emerging technology for cardiac imaging [10]. Currently CT offers spatial resolution as high as 500μm isotropic or more. The slice thickness is improved relative to standard MR imaging. CT is now clinically appropriate for studies of angiography, cardiac morphology, qualitative wall motion [11], and calcium scoring of the coronary arteries [12] and valve leaflets. This modality, however, is not suited to quantitative measures of regional wall mechanics, local myofibril orientation, or flow rates. Though, X-ray CT may ultimately provide the best diagnostic images of coronary vessel lumen morphology, there are potential drawbacks. There are two primary limitations associated with the use of X-ray CT. First, the associated radiation dose potentially makes serial or follow-up studies problematic [13]. Second, due to current hardware limitations, patients need to be administered blockers to decrease their heart rate below 60 beats per minute [14]. X-ray CT is also generally contraindicated for infants and children, a population that is frequently in need of quality tomographic images for the assessment of congenital heart defects.

MRI can characterize myocardial function through the use of cine MRI and tagged MRI. The latter provides a means to assess wall motion both qualitatively and

quantitatively. Tagging for qualitative purposes finds utility in the clinic for identifying regions of wall motion abnormality. Identification of wall motion abnormalities is useful for diagnosing the region and extent of coronary heart disease, ischemia, and infarction. Qualitative applications of myocardial tagging also include confirming pericardial restrictions [15]. The assessment of regional cardiac function aids the clinician in localizing diseases and assessing the extent and severity of myocardial dysfunction. For patients with coronary artery disease, congenital defects, and heart failure, diagnostic imaging plays a major role in the assessment of cardiac function and management of disease. Improvements in spatial and temporal resolution are some of the of active research area in MRI. It would provide more diagnostic images for coronary artery disease, small congenital defects, and micro-infarcts.

2.3.2 Cardiac Triggering

The heart is a constantly moving organ; therefore, acquiring cardiac data requires certain procedures in order to reduce the motion effects, which result from breathing process and beating heart motion. Gating or triggering is usually used to achieve this goal; in this process, an image for specific phase is acquired at a fixed time, and usually the R peak, where the heart is fully opened and minimum motion occurs is used to synchronize the MR signal for each cardiac cycle, so in each cardiac cycle there are a number of images that is acquired representing all phases that cover the whole cardiac cycle. This process is then repeated at each cardiac cycle to create the complete MR image for each phase. Cardiac cycle can be divided into any

number of phases depending on the purpose of the study; for more phases, however, the MRI procedure time increases. For example, electrocardiogram (ECG) signal can be used to synchronize the acquisition to obtain snapshot images of a beating heart from a plane of interest (Fig.2.4). The end diastole image of a live rat heart in Fig.2.5 was acquired with the monitoring and gating setup in our laboratory.

MRI is the only technique able to provide high resolution, quantifiable images encoding regional myocardial motion of the entire heart and, hence, is the modality of choice. MRI is, therefore, the essential method for exploring myocardial structure and function and their relationship.

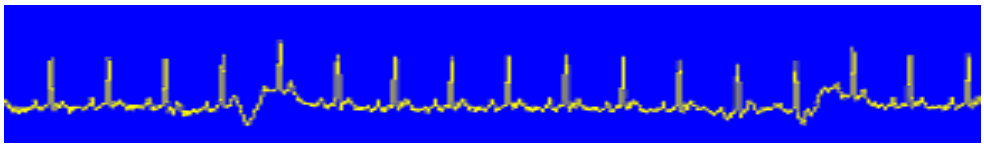

Figure 2.4: Electrocardiogram (ECG) signal of a beating normal rat heart.

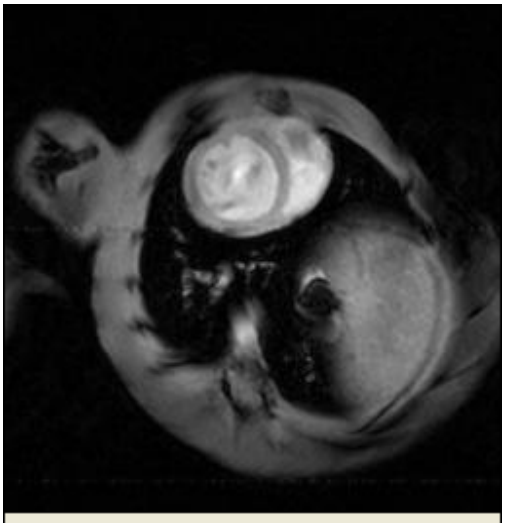

Figure 2.5: Short axis view of heart from a live rat acquired at diastole using cine MRI.

2.3.3 Cardiac Tagging

Cardiac MRI became a rapidly growing field with the use of tagged MRI (tMRI) in cardiac imaging to evaluate the regional cardiac wall motion. tMRI was first developed by Zerhouni [16] and then developed by Axel [17] as a way to track regional cardiac motion. Several techniques were introduced to create tags; among them, the spatial modulation of magnetization (SPAMM) technique is the most frequently implemented technique and the one that is usually used by most clinical scanners.

2.3.3.1 Spatial Modulation of Magnetization (SPAMM)

This method depends on a combination of RF pulses and short gradient waveforms to create periodic bands. The result is that the underlying tissue being imaged is marked with a plane of saturated protons, resulting in dark bands that deform as the underlying tissue deforms (Fig 2.6). These tissue bands can then be observed to move in consecutive cardiac gated images, and the underlying cardiac motion can be inferred using image processing techniques. The SPAMM technique can be appreciated by following a band of magnetization during the application of the SPAMM pulses. Starting with equilibrium magnetization (M_0) oriented along the z-axis (M_z), with both transverse components (M_x and M_y) equal to zero. After applying the first 90° RF pulse about the positive x-axis, the magnetization vectors become:

$$\begin{bmatrix} M_x \\ M_y \\ M_z \end{bmatrix} = -M_0 \begin{bmatrix} 0 \\ 1 \\ 0 \end{bmatrix} \tag{2.22}$$

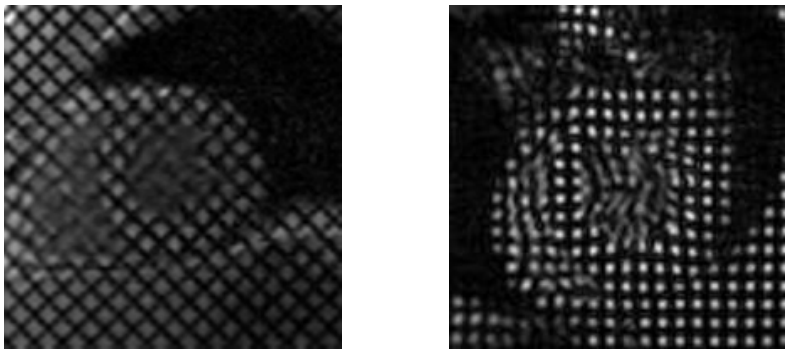

a b

Figure 2.6: Real tagged images for Left Ventricle at end diastolic phase of a) a healthy human and b) a healthy Rat LV, note different tags size, displacement, and direction of the tags

Application of a dephasing gradient results in the M_y magnetization being dephased in the *xy*-plane where the phase angle φ is determined by the equation:

$$\varphi = \gamma \int (\vec{G}(t).\vec{x})dt \tag{2.23}$$

Where $\vec{G}(t)$ represents the time varying magnetic field gradient that is applied (superposed) with the B_0 field to generate a variation in Larmor frequency at a position x. The combination of $\vec{G}(t)$ and B_0 field increases (or decreases) the Larmor frequency depending upon spatial location of spins . The ability to spatially modulate the local spins' phase and frequency is what allows for image formation via a technique referred to as Fourier spatial encoding.

$$\begin{bmatrix} M_x \\ M_y \\ M_z \end{bmatrix} = -M_0 \begin{bmatrix} \cos\varphi(\vec{x}) \\ \sin\varphi(\vec{x}) \\ 0 \end{bmatrix} \tag{2.24}$$

The magnetization can be restored to the *z*-axis through the application of another RF pulse of –90° about the *x*-axis, resulting in the following:

$$\begin{bmatrix} M_x \\ M_y \\ M_z \end{bmatrix} = M_0 \begin{bmatrix} -\cos\varphi(\vec{x}) \\ 0 \\ \sin\varphi(\vec{x}) \end{bmatrix} \tag{2.25}$$

Before imaging begins, the remaining transfer magnetization is being spoiled by large dephasing gradients. Perfect spoiling results in the following:

$$\begin{bmatrix} M_x \\ M_y \\ M_z \end{bmatrix} = M_0 \begin{bmatrix} 0 \\ 0 \\ \sin\varphi(\vec{x}) \end{bmatrix} \tag{2.26}$$

The net effect of the

$$90_{+x}^{0} \rightarrow G_{tag} \rightarrow 90_{-x}^{0}$$

steps is a spatially dependent modulation of the M_z magnetization. This process precedes the acquisition of image data and, therefore, results in a sinusoidal banding pattern in the acquired images. This scheme (Fig. 2.7) is referred to as a 1:-1 SPAMM preparation because the two RF pulses used were equal in magnitude and opposite in direction of rotation.

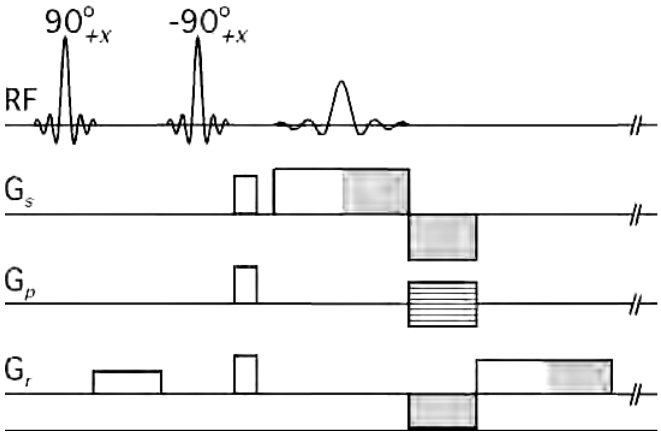

Figure 2.7: This figure diagrams a simple 1-1 SPAMM tagging pulse sequence followed by a gradient echo sequence. The $90^{0}_{+x} \rightarrow G_{tag} \rightarrow 90^{0}_{-x}$ sequence produces the tag banding pattern. The gradients that are used to crush the residual transverse magnetization are shown after the last RF tagging pulse on all three axes [18].

Chapter 3 : A Two Parameter Computational Model for the Left Ventricle Wall Motion Using tMRI

3.1 Computational Model for the LV Wall Motion

From the long axis view, the LV wall can be clinically divided into three parts. The upper, middle, and lower portions of LV are called the base, midventricle, and apex, respectively. During a cardiac cycle, the LV wall performs two simultaneous motions, the deformation along the short axis and the rotation along the long axis of LV. During systole, the apex rotates clockwise and the base rotates counter-clockwise as viewed from the base while both of them experience the deformation. This twist motion between the apex and base results in a torsion in the LV wall tissues. At the midventricle of a healthy heart, on the other hand, the rotational motion is negligible and the cardiac motion is dominated by the deformation that causes the radial and circumferential strains in the tissue. During diastole (systole), moreover, the LV wall at the midventricle experiences its smallest (largest) thickness. Without detailed information on the material property of the tissues, it is very difficult to develop a comprehensive mathematical model to simulate such a complicated LV wall motion. To simplify the problem, we consider only the two-dimensional motion, radial deformation and rotation, on a cross section (short-axis plane) of LV that is perpendicular to the long axis of LV. Let $\vec{r} = (x, y)$ and $\vec{r}' = (x', y')$ be the Cartesian coordinates of a point on the LV wall in the short-axis plane without (at end diastole) and with deformation or/and rotation,

respectively, where the origin of the coordinate is at the center (long axis) of LV. Note that $r = (x^2 + y^2)^{1/2}$ and $r' = (x'^2 + y'^2)^{1/2}$ are the distance to the center of LV without and with deformation or/and rotation, respectively. To describe the radial deformation, we use an isotropic deformation transformation,

$$\vec{r}' = (1 - \frac{\alpha^2}{r^2})\vec{r} \tag{3.1}$$

where α is the deformation parameter that characterizes the severity of the deformation. A larger α yields a more severe deformation. In this deformation model, the displacement of a point on the LV wall tissues along the short axis due to the deformation is $r' - r = -\alpha^2 / r$ where the minus sign represents the contraction of the LV wall during the cardiac motion. The 1/r-dependence of the deformation reflects a fact that the deformation near the center of LV (endocardium) is more severe than the deformation of the outer layer of the LV wall (epicardium). It should also be noted that this one-parameter isotropic deformation model can be extended to an anisotropic deformation model by replacing r^2 in Eq. (3.1) with a quadratic function of x and y with three coefficients. Such a three-parameters deformation function can describe the difference in the deformation of the LV wall tissues attached to the chest wall and the tissues attached to the septum. As a first-order approximation, in this study, we neglect the anisotropy of the deformation.

To describe the rotation of the LV wall in the short-axis plane, we propose a non-uniform two-dimensional rotational transformation,

$$\begin{aligned} x' &= x\cos\delta\theta - y\sin\delta\theta \\ y' &= x\sin\delta\theta + y\cos\delta\theta \end{aligned} \tag{3.2}$$

where the rotational angle is $\delta\theta = \beta / r$ and β is the rotation parameter. A positive (negative) β corresponds to a clockwise (counterclockwise) rotation. The 1/r-dependence of δθ is due to the fact that the rotation of the outer layer of the LV wall is smaller than the rotation of the tissue near the center of LV [19]. Note that large β value corresponds to larger rotation and β = 0 is of the case without any rotation. Combining Eqs. (3.1) and (3.2), one can calculate the displacement of the tissue at any given point in a short-axis plane of the LV wall during the cardiac motion as,

$$\begin{aligned} x' &= (1-\alpha^2/r^2)(x\cos\delta\theta - y\sin\delta\theta) \\ y' &= (1-\alpha^2/r^2)(x\sin\delta\theta + y\cos\delta\theta) \end{aligned} \tag{3.3}$$

where the deformation and rotation parameters α and β are determined by fitting (x′, y′) to the magnetization tag lines in the short-axis tMRI images of the LV wall. After the time-dependences of α and β are determined, Eq. (3.3) provides a model to map the motion of the LV wall tissues during the cardiac motion. It should be noted that in order to avoid the nonlinear entanglement of the two transformations in Eqs. (3.1) and (3.2), the non-uniform rotational transformation in Eq. (3.2) is applied before the deformation transformation in Eq. (3.1) since the 1/r-deformation is invariant under the rotational transformation but δθ changes with the application of the deformation function. The nonlinear entanglement could make the fitting of α and β complicated. For the algorithm of the fitting, one needs also the inverse transformation of Eq. (3.3) that can be easily obtained as:

$$x = \frac{1}{2}(1+\sqrt{1+4\alpha^2/r'^2})(x'\cos\delta\theta + y'\sin\delta\theta')$$
$$y = \frac{1}{2}(1+\sqrt{1+4\alpha^2/r'^2}(-x'\sin\delta\theta + y'\cos\delta\theta') \quad (3.4)$$

where $\delta\theta' = \beta / r'$.

3.2 tMRI Data Acquisition and Processing

3.2.1 Animal tMRI protocol

In this study, cardiac tMRI data were collected from six male Sprague-Dawley rats. Five of the rats were healthy and one was made diabetic with the procedures described in [20]. For MRI, the rats were anesthetized using 1.5% isofluorane in a mixture of 60% air and 40% oxygen. A 9.4 T horizontal bore scanner with a 60 mm radio frequency volume coil was used for MRI. ECG gated gradient echo based tagged images were collected for short-axis planes of the heart. The MRI machine parameters used in the experiment were: TR/TE= 25.00/2.44 ms, the number of averages = one, the field of view = 60 × 60 mm, and the image matrix = 256 × 256 pixels yielding an in-plane resolution of 234×234 μm. The grid size (distance between two neighboring tag lines) of the mesh of the magnetization tag lines was 0.8 mm and the width of each tag line was 0.3 mm. For MRI, the rat LVs were divided into 7 slices along the long axis as shown in Fig. 3.6 a and the thickness of the slice is 2.0 mm without any space between the slices. Five rats including a diabetic one were imaged at the midventricular level of their hearts and the remaining one was imaged near the apical and basal levels. All the images were taken from the view of the base so that the apex rotated clockwise and the base rotated counterclockwise in the

images. To study the LV wall motion in a full cardiac cycle, the cardiac cycle was divided into 10 equal-spaced phases and one tMRI image of the heart was acquired at each phase. The first phase was near end diastole when the LV was fully open and experienced little deformation and rotation while phase 5 was at end systole when the LV experienced the maximal deformation and rotation. All the experimental procedures were approved by the Institutional Animal Care and Use Committee at the University of Kansas Medical Center.

3.2.2 Human tMRI protocol

tMRI images of the human heart were taken from two healthy adults of 48 and 58 years old using a 1.5 T horizontal bore scanner with a body coil. ECG gated gradient echo based tagged images were collected for the short-axis planes of the heart. The MRI machine parameter used in the experiment were: TR/TE = 26.05/2.27 ms, the number of averages = one, the field of view = 350×400 mm, and the image matrix = 372×512 pixels yielding an in-plane resolution of 941×781 μm. The grid size of the mesh of the magnetization tag lines was 7.0 mm and the width of each tag line was 1.5 mm. For MRI, the human LVs were divided into 12 slices along the long axis and thickness of each slice was 8 mm without any space between the slices (see Fig. 3.6 b). For both cases, the images were acquired near the apex, midventricle, and base of LV. All the images are also from the view of the base so that the apex rotates clockwise and the base rotates counterclockwise in the images. To cover a full period of cardiac cycle, a cardiac cycle was divided into 13 equal-spaced phases for the first human case and 26 equal-spaced phases for the second case, respectively, and one

tMRI image was acquired at each phase. Similar to the rats, the first phase is near end diastole when the LV is fully open and experiences little deformation and rotation. One complication in tMRI of the human heart is the tag fading due to the use of a relatively low magnetic field which corresponds to a short relaxation time T_1 and a longer cardiac cycle as compared with the rat heart. Because of the relaxation of magnetization, the magnetization tag lines fade gradually and disappear after the transverse relaxation time T_1 [15]. For a magnetic field of 1.5 T, $T_1 \approx 0.8$ s and it is about the duration of a health adult cardiac cycle. The tag lines are therefore barely visible in the tMRI images near the end of a cardiac cycle.

3.2.3 tMRI Image Processing

The raw tMRI images of rats and human were acquired from the short-axis view of their entire heart and, sometime, of their entire bodies. The image of the LV wall, the data needed for studying the LV wall motion, occupies only a small portion of a raw image. In order to apply the computational model in Eq. (3.3) to the images, we need to crop and enlarge the region of interest of a raw image into a standard size so that the coordinates of the magnetization tag lines can be measured. To determine the magnification of the cropped images, the first frame in each series of stroboscopic tMRI images was used as the standard for all the images in that series. Note that this first frame in each series is the image near end diastole when LV is nearly fully open and experiences very little deformation and rotation. The first frame in each series of tMRI images was cropped by choosing a square box on the image that contains the LV wall and some of its surrounding tissues. The cropped image is centered with the

LV wall so that the origin of the coordinate in Eq. (3.3) is at the center of the image. The crop box created on the first frame was then used for cropping the rest frames in the same series of the tMRI images. After the cropping, all the images of the LV wall were enlarged by interpolation to a standard size of 256 × 256 pixels so that the coordinates of the mesh points of the magnetization tag lines can be conveniently measured in pixels. The enlargement of the cropped LV images reduces the quality of the images and widens the tag lines, but it does not alter the accuracy of the fitting since the accuracy of the measured coordinates of the tag lines depends only on the resolution of the original image and the width of the tag lines in the original image.

3.3 Model Fitting for the t-Dependence of α and β

To determine the deformation and rotation parameters α and β at different cardiac phases, the displacement of the LV wall tissues calculated from Eq. (3.3) was fitted successively to each frame of a series of stroboscopic tMRI images of the LV wall in a short-axis plane. In this study, the tMRI data of the LV wall motion at the midventricle as well as near the apex and the base were acquired from eight subjects including two healthy human and six healthy or diabetic rats.

Figure 3.1 is an example of tMRI images of the human and rat LV acquired in this study. The mesh of dark lines in the images are the magnetization tag lines. Note that the image resolution of the human LV in Fig. 3.1 is worse than that of the rats because the field of view used for the original image of the human heart is much larger than that used for the rats. For the fitting, an annular mesh of simulated tag lines was calculated from Eq. (3.3) with a given α and β as shown in Fig. 3.2 and

superimposed on the LV wall in a tMRI image. Note that the fitting for α and β should be done only with the tag lines that are attached to the LV wall tissues. The use of an annular shape of the calculated mesh excludes those irrelevant tag lines on the surrounding tissues or inside the LV cavity.

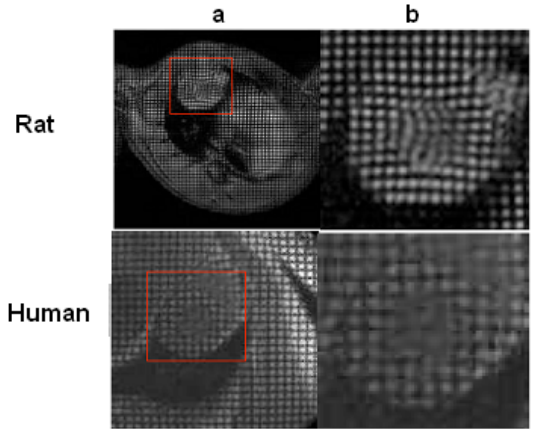

Figure 3.1: An example of the cropping and enlargement of tMRI images of the human and rat LV. (a) The raw images where the square box contains LV. (b) The cropped and enlarged image contained by the square box and used for the fitting of Eq. (3.3). The mesh of dark lines are the magnetization tag lines.

For the fitting, the grayscale intensity at each pixel is compared between the calculated mesh and the underlying tMRI image. Let $I_{\mathrm{mod}el}(x_i, y_i, \alpha, \beta)$ and $I_{image}(x_i, y_i)$ be the grayscale intensity of a pixel of the calculated mesh and of a tMRI image, respectively, where (x_i, y_i) is the coordinate of the pixel. The figure-of-merit function for the fitting is defined as:

$$F(\alpha,\beta) = \frac{1}{N}\sum_{i=1}^{N}\left[I_{\mathrm{mod}el}(x_i, y_i, \alpha, \beta) - I_{image}(x_i, y_i)\right]^2$$

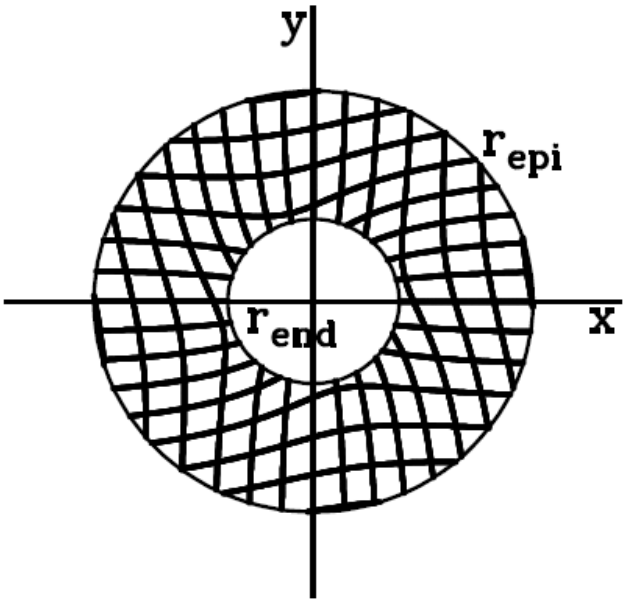

Figure 3.2: Example of annular mesh of simulated tag lines calculated from Eq. (3.3) where $\alpha/r_{epi} = 0.31$ and $\beta/r_{epi} = 0.14$. The inner and outer circles indicate the end diastolic radius of the LV wall at endocardium (r_{end}) and epicardium (r_{epi}), respectively.

where the summation is over all the pixels of the calculated mesh and N is the number of pixels of the mesh. As the grayscale intensity is 0 for black and 1 for white, $I_{model}(x_i, y_i, \alpha, \beta) = 0$ for all pixels of the calculated mesh while $0 \leq I_{image}(x_i, y_i) \leq 1$ for pixels of a tMRI image. Since the magnetization tags in a tMRI image are black lines, $F(\alpha, \beta) = 0$ corresponds to a perfect match between the calculated mesh and the magnetization tag lines at a pixel located at (x_i, y_i).

A minimization of F(α, β) thus yields a "best-fit" α and β. Due to a nonlinear dependence of β in Eq. (3.3), in this study, the fitting was processed iteratively and accomplished by using an in-house developed computer code. Figures 3.3-3.5 present examples of the fitted LV wall images at different cardiac phases where the

superimposed mesh of red lines were calculated using Eq. (3.3) with the "best-fit" α and β. In all the images, the calculated mesh fits very well with white or less-black dots on the LV wall. Note that those less-black dots are the tissues boxed by the magnetization tag lines. The model in Eq. (3.3) with the "best-fit" α and β therefore accurately describes the motion of the LV wall tissues. It should also be noted that the model fitting procedure developed here is very robust. Even in the case of the human heart near the end of a cardiac cycle where the tMRI images degrade significantly due to the original poor image quality and the tag fading, the computer fitting code was still able to match the calculated meshes with those barely-visible less-black dots in the images [see Figs. 3.3-3.5 (c)]. This demonstrates that

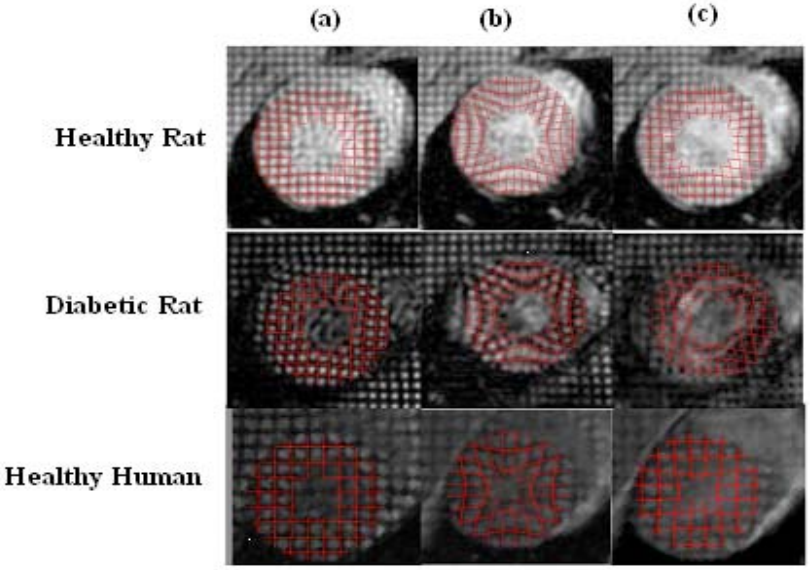

Figure 3.3: The fitted tMRI images of a healthy rat, diabetic rat, and human LV wall at the midventricle at (a) t = 0, the beginning of a cardiac cycle; (b) $t \approx 0.5\ T_{cardiac}$; and (c) $t \approx 0.9\ T_{cardiac}$; where $T_{cardiac}$ is the period of a cardiac cycle. The superimposed mesh of red lines was calculated using Eq. (3.3) with the "best-fit" α and β.

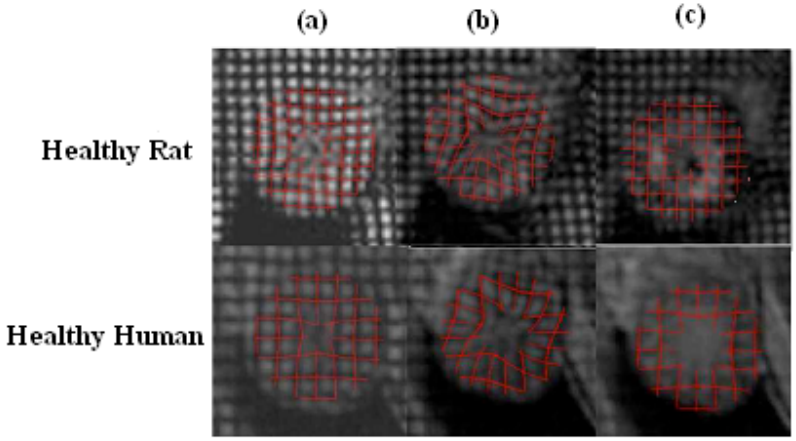

Figure 3.4: The same as Fig. 3.3 but of a healthy rat LV wall at slice 6 [see Fig. 3.6 (a)] and human LV wall at slice 9 [see Fig. 3.6 (b)].

it is not very demanding on the image quality of tMRI in using the model in Eq. (3.3) to describe the motion of the LV wall tissues.

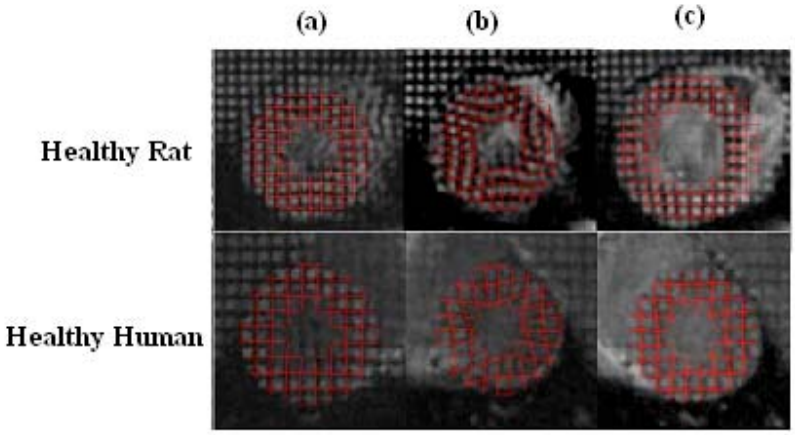

Figure 3.5: The same as Fig. 3.4 but of a healthy rat LV wall at slice 2 and human LV wall at slice 4.

3.4 Characterization of LV Wall Motion at the Midventricle

For the short-axis MRI of LV, in this study, the rat and human LVs were divided into 7 and 12 slices, respectively, along the long axis of LV as illustrated in

Fig. 3.6. For the rats, the tMRI data for LV at the midventricle were acquired at the 4th slice of LV [see Fig. 3.6 (a)]. In the case of human, the tMRI data for the midventricle is of the 6th slice of LV for human #1 and the 7th slice of LV for human #2 [see Fig. 3.6 (b)]. For a healthy heart, the LV wall tissues near the midventricle experience minimal rotation, i.e. $\beta \approx 0$ in Eq. (3.3). In Fig. 3.7, the "best-fit" deformation parameter α is plotted as a function of time during a cardiac cycle for the human and rat hearts, where α is scaled with the end diastolic radius of the LV wall at epicardium (r_{epi}) and time is scaled with the period of the cardiac cycle ($T_{cardiac}$). Among the subjects used in this study, $T_{cardiac} = 212 \pm 14$ ms for healthy rats, $T_{cardiac} =$ 235 ms for the diabetic rat, and $T_{cardiac} = 830$ ms for human. Compared with the end

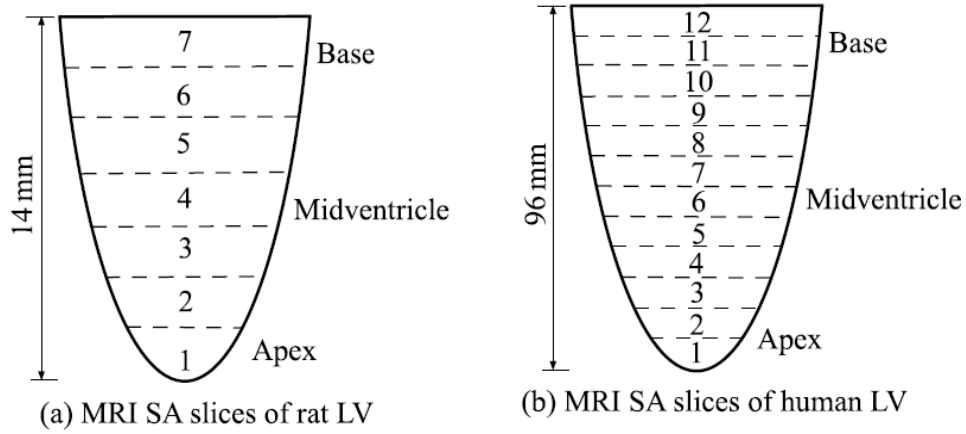

Figure 3.6: The sketches of the MRI short-axis slices of LV along the long axis for (a) rats and (b) human, where the number on each slice labels the slice.

diastolic radius of the LV wall at endocardium (r_{end}), r_{epi} can be better estimated from MRI images because of the difficult in distinguishing the endocardial tissues from the blood inside the LV cavity. The end diastolic radius r_{epi} is therefore used here to scale α so that LVs with different sizes can be compared. Note that $(\alpha/r_{epi})^2$ represents the

relative deformation of the LV wall at epicardium. Table 3.1 lists the values of r_{epi} and r_{end} for the subjects used in this study. For the cases of healthy rats and human, the average values of α is plotted in Fig. 3.7 and the error bars on the curve are the maximal deviation of α within each group. Because of a very limited number of subjects in this study, the error bars here does not have much statistical significance. They are only used for showing the deviation of the data. In all three cases (healthy human, healthy rat, and diabetic rat), α increases during the systolic motion($t \leq 0.5$ $T_{cardiac}$) and decreases during the diastolic motion ($t \geq 0.5$ $T_{cardiac}$). This is consistent with the fact that LV contracts during systole, relaxes during diastole, and the largest deformation occurs near end systole ($t > 0.5$ $T_{cardiac}$). Note that α^2/r_{end} is the change in the radius of the LV cavity in the short-axis plane and therefore α^2 is proportional to the reduction of the volume of the LV cavity due to the LV contraction. Compared with the healthy human and rat hearts, the value of α/r_{epi} of the diabetic rat is higher when $t \geq 0.3$ $T_{cardiac}$. This could suggest that the diabetes may result in a larger stress and a slower relaxation in LV wall tissues during the cardiac cycle.

Such a diabetes-induced dysfunction of the LV wall has also been observed before [20, 21]. The fitting of Eq. (3.3) to the images of the diabetic rat also revealed that $\beta = 6$ at the midventricle as shown in Fig. 3.8. The LV wall motion of a diabetic heart therefore contains a significant rotational component at the midventricle. The

rotational direction is the same as that of the apex (clockwise as viewed from

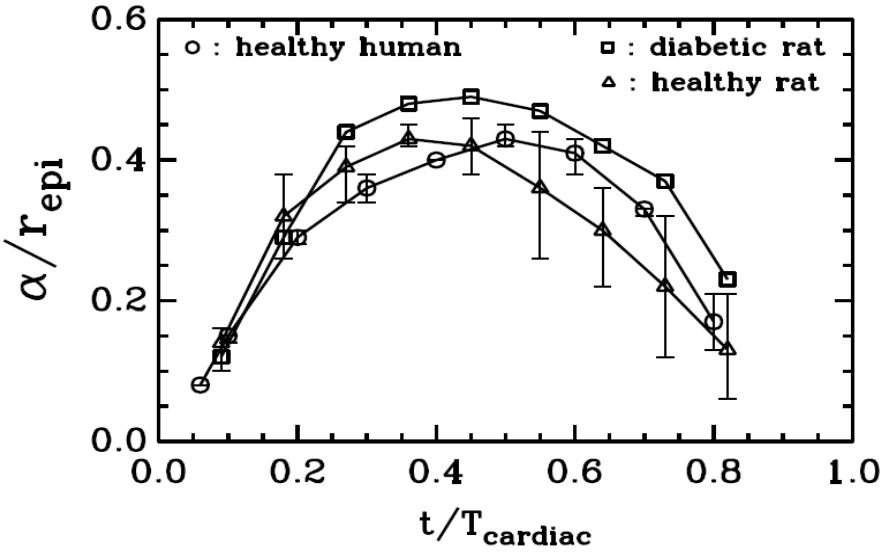

Figure 3.7: The deformation parameter as a function of time during a cardiac cycle for the human (circle), healthy rat (triangle), and diabetic rat (square) LV at the midventricle, where r_{epi} is the end diastolic radius of the LV wall at epicardium and $T_{cardiac}$ is the period of the cardiac cycle.

the base). Unlike the rotation at the apex or the base (see the next section), the rotation at the midventricle of diabetic rat occurs only during systole and it becomes untwisted near end systole ($t \approx 0.5\ T_{cardiac}$). Compared with a healthy heart, this rotational motion at the midventricle is significant and could be developed into a clinical marker for diagnose of heart dysfunction. These characteristics of the LV wall motion of diabetic heart need to be further studied with more subjects for better statistics.

3.5 Characterization of LV Wall Motion Near the Apex and the Base

Away from the midventricle, the LV wall motion in general consists of both the deformation and rotational components. Figures 3.9 and 3.10 plot α and β near the apex and the base as functions of time

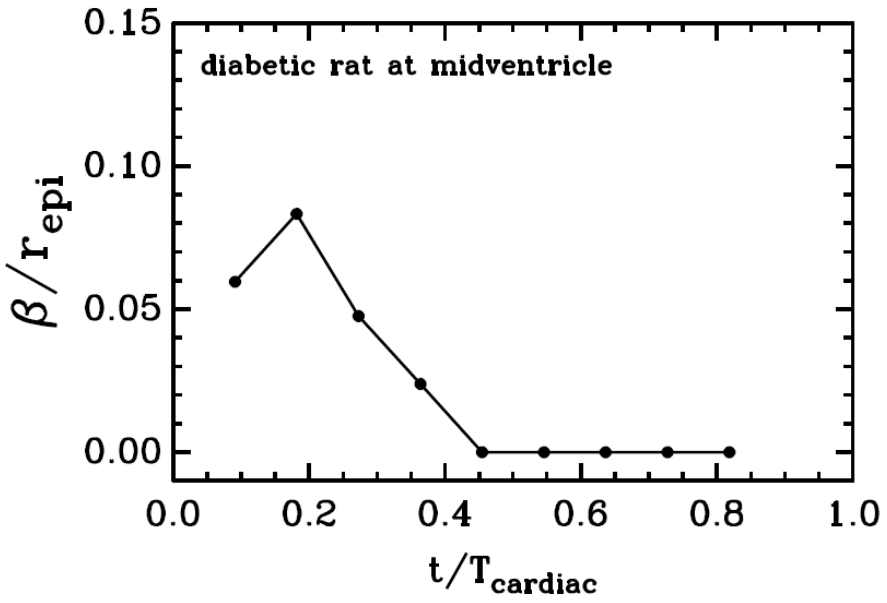

Figure 3.8: The rotation parameter as a function of time during a cardiac cycle for the diabetic rat LV at the midventricle, where r_{epi} is the end diastolic radius of the LV wall at epicardium and $T_{cardiac}$ is the period of the cardiac cycle.

during a cardiac cycle, where both α and β are scaled with r_{epi} so that hearts with different sizes can be compared. The values of r_{epi} near the apex and the base are also listed in Table 3.1. As shown in the figures, the deformation and rotation near the apex are larger than that near the base in both cases of human and rat. This observation is consistent with other studies [22, 23]. As the apex and the base rotate in opposite directions, the LV wall tissues experience a twist or torsion during the cardiac motion. The torsion of the LV wall is the average twist angle between the

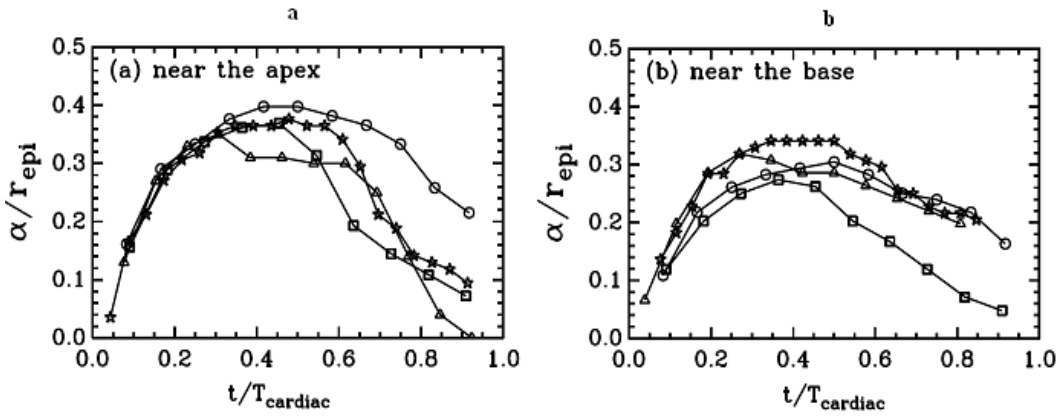

Figure 3.9: The deformation parameter as a function of time during a cardiac cycle near (a) the apex and (b) the base. Squares are of a healthy rat at (a) the 2nd and (b) the 6th slice of LV. Circles are of human #1 at (a) the 4th and (b) the 9th slice of LV. Triangles are of human #1 at (a) the 5th and (b) the 8th slice of LV. Stars are of human #2 at (a) the 2nd and (b) the 8th slice of LV

apex and the base (twist angle per length) and characterizes a shear stress in the LV wall tissues along the long axis. In calculation of the torsion, however, the base rotation was neglected in some of previous studies for a simplification of the problem. Having an analytic model of the LV wall motion in Eq. (3.3), the approximation of neglecting the base rotation is no longer necessary here and the twist angle and torsion can be calculated more accurately. For this purpose, we rewrite Eq. (3.3) in the polar coordinate as $r' = r - \alpha^2 / r$ and $\theta' = \theta + \delta\theta$, where $(x, y) = (r\cos\theta, r\sin\theta)$ and $(x', y') = (r'\cos\theta', r'\sin\theta')$. The twist angle between the apex and base can be simply calculated as:

$$\phi = \delta\theta\big|_{apex} - \delta\theta\big|_{base} = \left(\frac{\beta}{r}\right)_{apex} - \left(\frac{\beta}{r}\right)_{base} \quad (3.6)$$

Table 3.1: The end diastolic radii of the LV wall at endocardium (r_{end}) and epicardium (r_{epi}). The unit of the radius is mm. Rat 1-5 are healthy rats and rat 6 is the diabetic one. The radii were estimated from MRI images. See Fig. 3.6 for the numbering of slices.

Midventricle		r_{end}	r_{epi}	r_{epi}/r_{end}
human 1	slice 6	12.5	29.5	2.36
human 2	slice 5	13.4	30.8	2.31
rat 1	slice 4	2.8	6.5	2.27
rat 2	slice 4	3.4	7.7	2.28
rat 3	slice 4	2.6	5.9	2.25
rat 4	slice 4	3.0	6.5	2.14
rat 6	slice 4	2.5	6.0	2.36
Near Apex or Base		r_{end}	r_{epi}	r_{epi}/r_{end}
human 1	slice 4	11.1	25.2	2.27
	slice 5	12.5	27.1	2.17
	slice 8	14.8	31.4	2.12
	slice 9	14.8	31.8	2.15
human 2	slice 2	13.0	26.9	2.07
	slice 8	16.0	34.3	2.14
rat 5	slice 2	2.2	4.4	2.00
	slice 6	2.8	5.8	2.07

where (β/r) apex and (β/r) base are the values of β/r at the apex and the base levels, respectively. The torsion can then be obtained from $\tau = \varphi/L$, where L is the distance along the long axis between the apex and the base levels. In Eq. (3.6), the ranges of

value of r at the apex and the base are different because of different cross-sectional sizes of the LV wall at different short-axis planes. In order to factor out this different scale of r, we introduce a dimensionless scaled radial coordinate $\rho = (r - r_{end})/(r_{epi} - r_{end})$. The range of the value of ρ is always [0, 1] as r varies from the endocardium radius r_{end} to the epicardium radius r_{epi} in any short-axis plane.

The torsion can be expressed as a function of ρ as where C_a and C_b are the values of $C = \beta/r_{epi}$ at the apex and at the base, respectively, and λ_a and λ_b are the values of $\lambda = r_{end}/r_{epi}$ at the apex and at the base, respectively. In Eq. (3.7), the time dependence of τ is from the time dependence of β/r_{epi} during a cardiac cycle (see Fig. 3.10).

$$\tau = \frac{1}{L}\left[\frac{C_a}{(1-\lambda_a)\rho + \lambda_a} - \frac{C_b}{(1-\lambda_b)\rho + \lambda_b}\right] \qquad (3.7)$$

Because $C_a > 0$, $C_b < 0$, $\lambda_a < 1$ and $\lambda_b < 1$, at any given time during a cardiac cycle, the maximal τ is at endocardium (ρ = 0) and the minimal τ is at epicardium (ρ = 1). It should be noted that Eq. (3.7) can also be used to calculate the torsion between any two short-axis planes of a LV. To calculate the torsion between LV slice i and slice j in Fig. 3.6, for example, C_a and λ_a are the values of β/r_{epi} and r_{end}/r_{epi} evaluated at slice i and, similarly, C_b and λ_b are the values at slice j. In Fig. 3.11, τ as a function of ρ is plotted for the cases of the rat and human #1 between slice 4 and slice 9 in Fig. 3.10 at $t \approx 0.4\ T_{cardiac}$ for the rat and $t \approx 0.5\ T_{cardiac}$ for human. In both cases, τ plotted is close to the maximal torsion of the LV wall during a cardiac cycle at each given ρ. The ρ-dependences of τ at other t are similar to the curves in Fig. 3.11 but at a lower

overall value. In calculating τ , L = 40 mm for human and L = 8 mm for rat. The values of r_{epi} and r_{end} are listed in Table 1. As shown in Fig. 3.11, the torsion on the

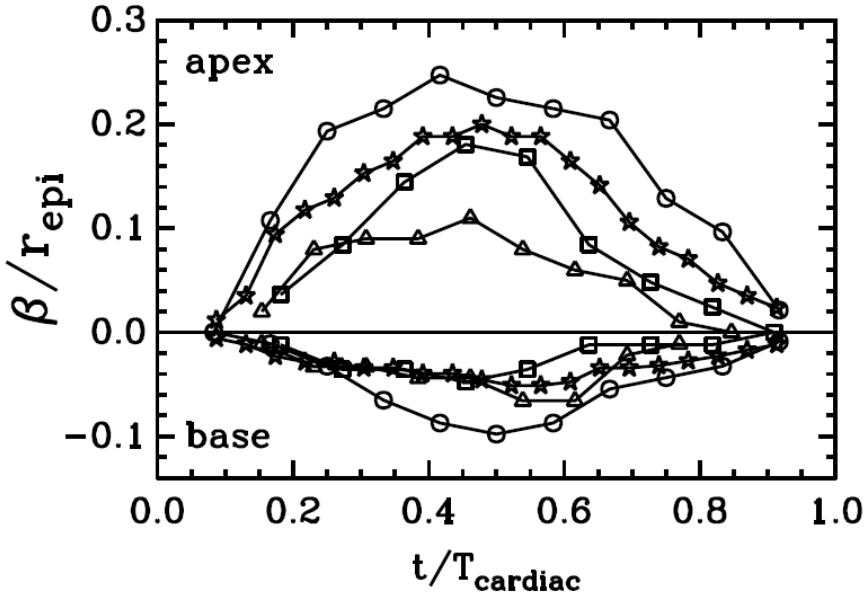

Figure 3.10: The same as Fig.3.9 but β vs. t during a cardiac cycle near the apex (β > 0) and the base (β < 0).

rat heart is significantly larger than that on the human heart. This difference in τ is mainly due to different sizes (L) of their hearts. In these two cases, the maximal twist angle of the LV wall at the endocardium is $\varphi_{max} \approx 0.45$ rad for the rat and $\varphi_{max} \approx 0.7$ rad for human.

One interesting phenomenon observed in this study is a constant ratio of the torsion (τ_{end}) or twist angle (φ_{end}) at endocardium to the torsion (τ_{epi}) or twist angle (φ_{epi}) at epicardium. From Eq. (3.7)

$$\phi_{end} = \tau_{end} L = C_a / \lambda_a - C_b / \lambda_b \quad \text{and} \quad \phi_{epi} = \tau_{epi} L = C_a - C_b$$

The ratio of these maximal and minimal torsion can be written as

$$\eta = \frac{\tau_{end}}{\tau_{epi}} = \frac{\phi_{end}}{\phi_{epi}} = \frac{1}{\lambda_b} + \left(\frac{\lambda_b - \lambda_a}{\lambda_a \lambda_b} \right) \frac{C_a}{C_a - C_b} \qquad (3.8)$$

Note that $\lambda = r_{end} / r_{epi}$ is the ratio of the end diastolic radii of the LV wall at

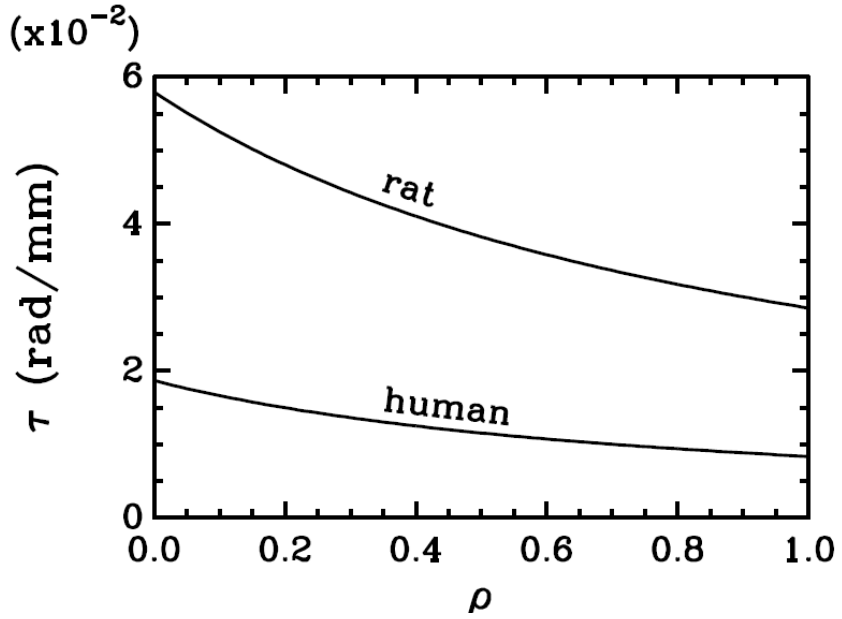

Figure 3.11: The torsion of LV wall as a function of radial distance from the endocardium to the epicardium for the cases of rat and human #1 in Fig. 3.10. For human #1, τ was calculated between LV slice 4 and 9 (see Fig. 3.6) and at $t \approx 0.5\ T_{cardiac}$. For the rat, τ is at $t \approx 0.4\ T_{cardiac}$.

endocardium and epicardium. Since the difference in λ at different short-axis planes of a LV wall is fairly small (see Table I), $(\lambda_b - \lambda_a)/\lambda_a << 1$ then the constant term of $1/\lambda_b$ is the dominant term in Eq. (3.8). During the cardiac motion, therefore, η depends on t very weakly. Compared with the strong t-dependence of β (see Fig. 3.10), η can be considered as a constant during the cardiac motion, i.e.

$$\eta \approx \frac{1}{\lambda_b} = \frac{r_{epi}}{r_{end}} \qquad (3.9)$$

Figure 3.12 plots η as a function of t for the cases of Fig. 3.10 and confirms Eq. (3.9). Moreover, the values of η for rat and human are found to be very close. This is because the values of r_{epi}/r_{end} are very similar for rat and human and are also very similar at different short-axis planes of a LV (see Table 3.1). Considering that τ varies with time substantially during a cardiac cycle and the values of τ are very different for rat and human, this constant of the cardiac motion is significant. To our knowledge, this constant of the cardiac motion has never been observed before. Further study

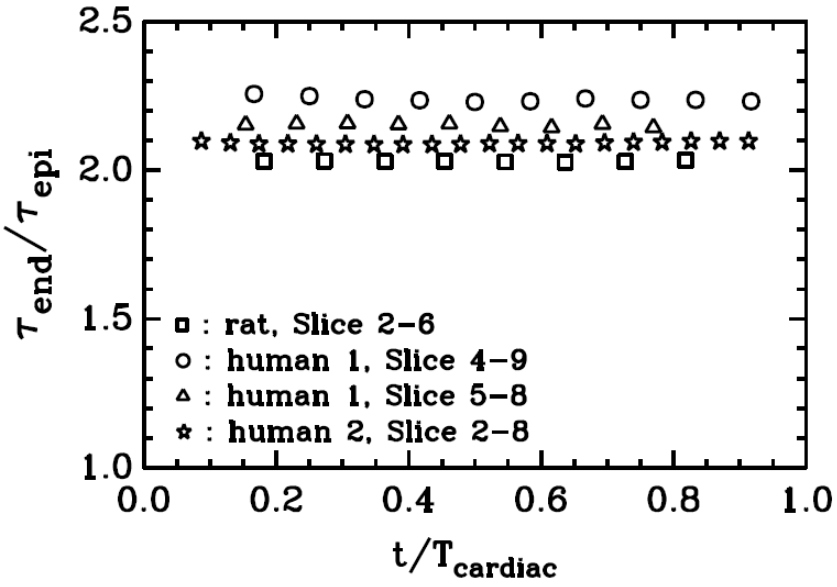

Figure 3.12: Ratio of the torsion at endocardium and at epicardium as a function of time during a cardiac cycle for the cases in Fig. 3.10.

with more subjects, especially with diseased heart, is certainly needed in order to test the generality and to understand the physiological importance of this constant.

3.6 Mapping of Mechanical Strain of LV Wall Tissues:

Another advantage of using the analytic model in Eq. (3.3) to study the LV wall motion is that the mechanical strain [24, 25] of the LV wall tissues in short-axis plane can be easily calculated analytically at different phases of a cardiac cycle without numerical interpolation of tMRI data. Let $\delta\vec{r} = (\delta x, \delta y) = (x'-x, y'-y)$ be the displacement vector of the LV wall tissues in a short-axis plane due to the cardiac motion. In the Cartesian coordinate, the displacement gradient tensor in the short-axis plane can be calculated from Eq. (3.3) as

$$\frac{\partial \delta x}{\partial x} = U_1(\rho)\cos(2\theta + \delta\theta) + \left[\sin\delta\theta + \sin(2\theta + \delta\theta)\right]U_2(\rho) + \cos\delta\theta - 1 \tag{3.10}$$

$$\frac{\partial \delta x}{\partial y} = U_1(\rho)\sin(2\theta + \delta\theta) + \left[\cos\delta\theta + \cos(2\theta + \delta\theta)\right]U_2(\rho) - \sin\delta\theta \tag{3.11}$$

$$\frac{\partial \delta y}{\partial x} = U_1(\rho)\sin(2\theta + \delta\theta) - \left[\cos\delta\theta + \cos(2\theta + \delta\theta)\right]U_2(\rho) + \sin\delta\theta \tag{3.12}$$

$$\frac{\partial \delta y}{\partial y} = -U_1(\rho)\cos(2\theta + \delta\theta) + \left[\sin\delta\theta - \sin(2\theta + \delta\theta)\right]U_2(\rho) + \cos\delta\theta - 1 \tag{3.13}$$

Where

$$U_1(\rho) = \frac{\alpha^2}{r^2} = \frac{(\alpha / r_{epi})^2}{\left[(1-\lambda)\rho + \lambda\right]^2} \tag{3.14}$$

$$\delta\theta = \frac{\beta}{r} = \frac{(\beta / r_{epi})}{(1-\lambda)\rho + \lambda} \tag{3.15}$$

$$U_2(\rho) = \frac{1}{2}\delta\theta[1 - U_1(\rho)] \tag{3.16}$$

In Eqs. (3.10)-(3.16), x and y are substituted by its polar coordinate $x = r\cos\theta$ and $y = r\sin\theta$, and r is substituted by ρ. The Green-Lagrange strain tensor in a short-axis plane can then be calculated in term of the deformation gradient tensor [29,30] as

$$\mathbf{E} = (\mathbf{F}^T\mathbf{F} - \mathbf{I})/2$$

where the deformation gradient tensor is defined as

$$\mathbf{F} = \mathbf{I} + \frac{\partial \delta \vec{r}}{\partial \vec{r}}$$

The components of the strain tensor E are therefore

$$E_{ij} = \frac{1}{2}\left(\frac{\partial \delta z_i}{\partial z_j} + \frac{\partial \delta z_j}{\partial z_i} + \frac{\partial \delta z_1}{\partial z_i}\frac{\partial \delta z_1}{\partial z_j} + \frac{\partial \delta z_2}{\partial z_i}\frac{\partial \delta z_2}{\partial z_j} \right) \tag{3.17}$$

where z_1 = x, z_2 = y and the index i and j have the range of (1, 2). Note that the infinitesimal strain tensor (Cauchys strain tensor) can also be easily calculated as the first two terms of the right-hand side of Eq. (3.17). The infinitesimal strain is a linear approximation of the Green-Lagrange strain, which is only valid for small deformation. The Green-Lagrange strain tensor is more appropriate for a measure of large deformation of the LV wall tissues during the cardiac motion. Due to the cylindrical symmetry of a LV, the Green-Lagrange strain tensor in the polar coordinate is more convenient for measuring the deformation of the LV wall in a short-axis plane and can be obtained through the coordinate transformation,

$$\begin{pmatrix} E_{rr} & E_{r\theta} \\ E_{r\theta} & E_{\theta\theta} \end{pmatrix} = T^{-1} \begin{pmatrix} E_{11} & E_{12} \\ E_{21} & E_{22} \end{pmatrix} T \tag{3.18}$$

Where T is the transformation between the Cartesian and polar coordinates

$$(\vec{e}_x, \vec{e}_y) = T(\vec{e}_r, \vec{e}_\theta)$$

$$T = \begin{pmatrix} \cos\theta & -\sin\theta \\ \sin\theta & \cos\theta \end{pmatrix} \tag{3.19}$$

The radial (E_{rr}) and the circumferential ($E_{\theta\theta}$) strains are

$$E_{rr} = \frac{1}{2}(E_{11} + E_{22}) + \frac{1}{2}(E_{11} - E_{22})\cos 2\theta + E_{12}\sin 2\theta \tag{3.20}$$

$$E_{\theta\theta} = \frac{1}{2}(E_{11} + E_{22}) - \frac{1}{2}(E_{11} - E_{22})\cos 2\theta - E_{12}\sin 2\theta \tag{3.21}$$

When $\beta=0$

$$E_{rr} = U_1 + \frac{1}{2}U_1^2 \tag{3.22}$$

$$E_{\theta\theta} = -U_1 + \frac{1}{2}U_1^2 \tag{3.23}$$

Both of the radial and circumferential strains are therefore independent of θ at the midventricle level of a healthy heart where LV wall tissues experience minimal rotation. Figure 3.13 plots E_{rr} and $E_{\theta\theta}$ as functions of ρ at the midventricles of the healthy rat and human LV and diabetic rat LV at end systole ($t > 0.5\ T_{cardiac}$) when the largest deformation occurs. The strains calculated at other t are similar to the curves in Fig. 3.13 except that the overall amplitudes of the strains are lower. In Fig. 3.13, a positive E_{rr} and a negative $E_{\theta\theta}$ indicate that the LV wall tissues undergo a stretch in the radial direction and a contraction in the circumferential direction during the cardiac motion. For the healthy rat and human, the amplitudes of E_{rr} and $E_{\theta\theta}$ decrease monotonically when ρ varies from endocardium to epicardium. In these cases, the terms that are linear in U_1 are dominant in Eqs. (3.22) and (3.23). For the diabetic rat, however, the maximal $E_{\theta\theta}$ is away from endocardium because the second term (U_1^2)

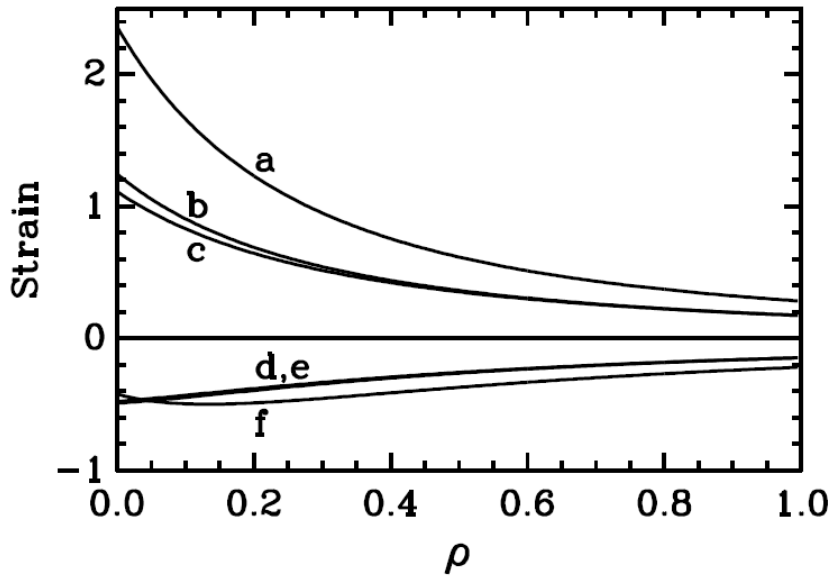

Figure 3.13: E_{rr} and $E_{\theta\theta}$ as functions of ρ for the cases in Fig. 3.7 at their maximal α. Curve a is E_{rr} of diabetic rat, curve b is E_{rr} of human, curve c is E_{rr} of healthy rat, curve d and e are $E_{\theta\theta}$ of healthy rat and human, and curve f is $E_{\theta\theta}$ of diabetic rat. Curve d and e are overlapped.

in Eq. (3.23) becomes important when the deformation is large. Moreover, Fig. 3.13 shows that the strains in the diabetic heart wall tissues are significantly higher than that of healthy hearts. This observation is in a good agreement with other studies [26]. The increase of the strains in a diabetic heart during the cardiac motion is probably due to the stiffness of the fibers of a diabetic heart. Since E_{rr} and $E_{\theta\theta}$ in Eqs. (3.20) and (3.21) only weakly depend on β, Eqs. (3.22) and (3.23) are also the dominant terms of the radial and circumferential strains in any short-axis plane of a LV and the ρ-dependences of the strains at the apex and base are very similar to those in Fig. 3.13. With Eqs. (3.22) and (3.23) or Eqs. (3.20) and (3.21), the variations of the strains during a cardiac cycle can also be easily calculated with obtained t-dependences of α and β in Figs 3.7-3.10. Another quantity that is useful in assessing

cardiac function is the strain rate [27]. The strain rate is the velocity of the deformation and related to the stress of the LV wall tissues. It can be calculated from Eqs. (3.22) and (3.23) as

$$\frac{dE_{rr}}{dt} = (1 + U_1)\frac{2(\alpha / r_{epi})}{[(1-\lambda)\rho + \lambda]^2}\frac{d}{dt}\left(\frac{\alpha}{r_{epi}}\right) \tag{3.24}$$

$$\frac{dE_{\theta\theta}}{dt} = -(1 - U_1)\frac{2(\alpha / r_{epi})}{[(1-\lambda)\rho + \lambda]^2}\frac{d}{dt}\left(\frac{\alpha}{r_{epi}}\right) \tag{3.25}$$

where dα/dt can also be obtained from the t-dependence of α in Figs. 3.7 and 3.9 by simply using a polynomial fitting. Note that the fitting of a α-t curve can be much easier and better accomplished with a lesser number of tMRI images in a cardiac cycle as compared with a direct interpolation of the tMRI images for the strain rate.

Chapter 4 : MRI Studies on the Global Functions of the Left Ventricle

Heart Failure is a highly prevalent disease syndrome in industrialized countries. Myocardial diseases can be understood easily by studying the cardiac function; consequently, diagnostic imaging plays a significant role in the assessment of the cardiac function and in the management of those diseases. Diabetes mellitus has been identified as an etiologic factor in the development of heart failure, in particular diastolic heart failure, and the incidence of diabetes mellitus in patients with ischemic cardiomyopathy is markedly increased [28]. Global and regional (local) parameters are usually used to evaluate the cardiac function for diagnostic purposes. General volumetric measures characterize the global parameters and include: cardiac volume, stroke volume, ejection fraction, cardiac output, and flow velocity. The regional parameters are those which are used for characterizing local myocardial deformation and motion like wall thickening, strain, and strain rate.

Cardiac function analysis is the method that is widely used for calculating the global and the regional (local) cardiac parameters. These parameters depend mainly on the heart segmentation process. However, complexities of the heart shape and motion patterns add another challenge to these analyses. Because it is the largest chamber of the heart and being responsible for the pumping of the oxygenated blood to the entire body, in most cardiac studies, left ventricle is considered as an indicator of the cardiac function. The evaluation of the left ventricular (LV) performance plays

a significant role in diagnosis, treatment planning, and in the follow-up of patients with heart diseases.

4.1 Global LV Functions

For clinical purposes, end-diastolic volume (EDV), end-systolic volume (ESV), and ejection fraction (EF) are usually used to evaluate the performance of the LV. These parameters are known as the global parameters of the LV function. Furthermore, the LV function can be quantitatively assessed through the analysis of the phase–volume curve, which represents LV volume at multiple phase points throughout the cardiac cycle. Dysfunction of LV diastolic function is one of the earliest manifestations of cardiac problem and usually precedes systolic dysfunction in many cardiac diseases [29, 30].

Ciné magnetic resonance imaging technique (ciné MRI) can be used to evaluate cardiac performance in diabetic animals to a high accuracy by calculating the cardiac global parameters, such as end-diastolic and end-systolic volumes, stroke volume, ejection fraction, and cardiac output. The LV volume can be measured using contiguous short axis views of the heart. End-diastolic (end-systolic) volume is found by the summation of the areas of the maximum (minimum) LV opening in each phase (Fig 4.1), followed by multiplying this summation by the slice thickness. Stroke

$$V_{ed} = \sum_{n} Enddiastolic.area \times slice.thickness \tag{4.1}$$

$$V_{es} = \sum_{n} Endsystolic.area \times slice.thickness \tag{4.2}$$

volume (SV) is one of the most significant parameters which physicians usually consider as a sign of cardiac dysfunction. It is defined as the volume of blood ejected

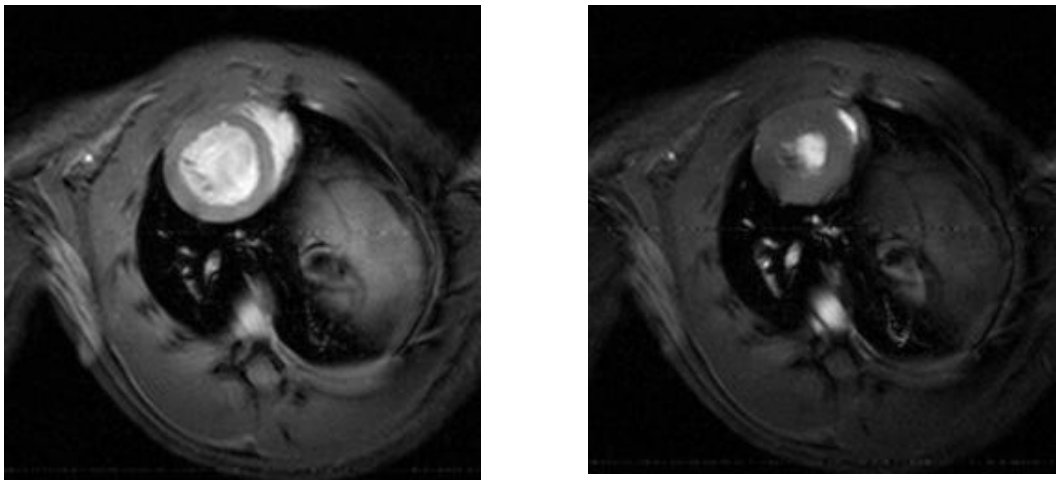

Figure 4.1: Two ciné images of the left ventricle of healthy rat at end diastole and end systole phases (blood white), respectively.

during one heart beat and it is also related to the end diastole volume V_{ed} (the volume of the heart at the end of filling or expansion), and the end systole volume V_{es} (the volume of the heart after ejection or contraction) by the relation:

$$SV = V_{ed} - V_{es} \tag{4.3}$$

Ejection fraction (EF) is the most common measurement of the cardiac performance; it can be used as a standard index for the assessment of the cardiac function. EF can be defined as the relative portion of the end diastolic volume ejected during one heart beat, and it can be calculated by the following equation:

$$EF(\%) = \frac{V_{ed} - V_{es}}{V_{ed}} \times 100 \ . \tag{4.4}$$

LV systolic dysfunction is usually occurs when EF < 50 [31]. The third parameter in cardiac function is the cardiac output (CO), which is the volume of the blood ejected

per unit time. It is related to the stroke volume and to the heart rate (HR) by the relation:

$$CO = SV \times HR \tag{4.5}$$

The last significant global parameter that can be used to assess cardiac function is the left ventricle mass, which can be calculated by the fundamental relationship:

$$m = V \times d \ ,$$

where m is tissue mass, V is tissue volume, and d is tissue density. Knowing that the tissue density is about 1.05 g/cm^3, and the LV volume is the difference between the inner (endo) and the outer (epi) volume of the LV. The LV mass equation can be written as:

$$LVm = 1.05(V_{ed} - V_{es}) \tag{4.6}$$

4.2 Cardiac Dysfunction In The Diabetic Rat: Quantitative Evaluation Using High Resolution Magnetic Resonance Imaging

Diabetic cardiomyopathy (DCM) is characterized by a series of myocardial changes in diabetes mellitus: such as fibrosis, hypertrophy and microcirculatory abnormalities. These cardiovascular problems reduce cardiac performance and eventually cause cardiac failure. A high occurrence of cardiac failure is seen in individuals with diabetic cardiovascular complications [32]. DCM is distinguished by an early diastolic dysfunction in the disease development [26, 33, 34]. In addition, reports also suggest slight systolic dysfunction later during the course of diabetes that evades detection with echocardiography [33].

Magnetic resonance imaging (MRI) has proven to be a powerful noninvasive imaging modality for structural and functional evaluation of the rat heart [35]. However, in vivo cardiac MRI studies using diabetic rat models are very limited. Understanding the course of pathological changes in an appropriate model is the key for developing therapeutic strategies to prevent heart failure. In order to evaluate the cardiac performance in vivo we used ciné MRI, a robust technique for providing cardiac functional information and the reference standard for real time three-dimensional imaging of myocardial structure [36,37]. In a previous study, Loganathan and colleagues [38] demonstrated the merits of high-resolution MRI in visualizing the diabetic heart and characterized the structural properties of non-beating myocardial tissue in the STZ-diabetic Sprague-Dawley rat. As an extension of the previous study, we have characterized the cardiac dysfunction associated with diabetes in this model. In particular, we report quantitative measurements on left ventricular end-diastolic and end-systolic volumes and demonstrate that these parameters are different for STZ-diabetic Sprague-Dawley rats when they are compared with healthy rats.

(a) Procedures and MRI protocols

After 8 weeks of diabetes, an ECG gated cardiac MRI scan was performed for 12 rats (6 healthys and 6 diabetic) using high resolution 9.4 T horizontal bore scanner at Hoglund Brain Imaging Center (HBIC), University of Kansas Medical Center (UKMC), to evaluate left ventricle global parameters function. The ECG gated gradient-echo-based sequence was used to acquire ciné images of the cardiac cycle

from the short axis view of the heart over 10 equally incremented intervals with the following parameters: TR/TE=25/2.44 ms, number of averages=1, image matrix=128 x 128, field of view=60mm x 60mm, number of slices=1, and slice thickness=2.0 mm. The image acquisition was repeated six times by moving the slice location to completely encompass the LV cavity from the apex to the base (Fig 4.2). Image J software [38] was used to analyze the images . The area of each slice was found by tracking the blood boundaries on the left ventricle. The area then was converted from pixel to mm^2 using the conversion factor of (60X60) mm^2 / (128X128) pixel which is 0.22 mm^2 / pixel.

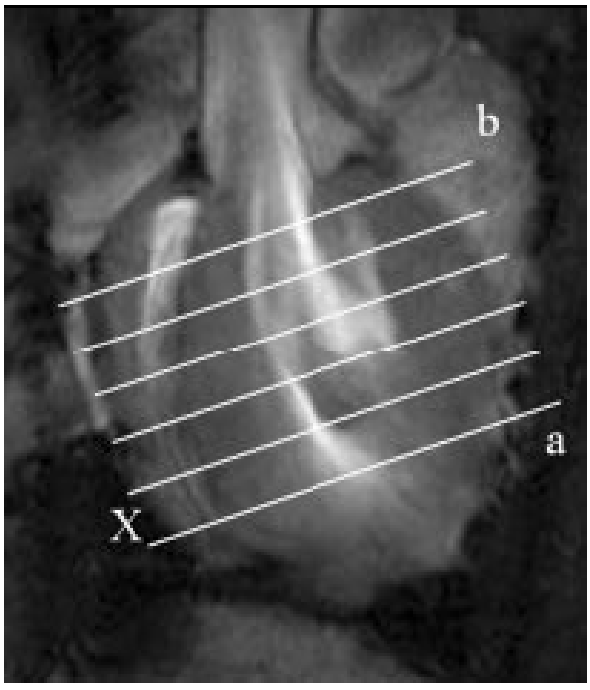

Figure 4.2: Illustration of the left ventricular (LV) long axis view. LV was spatially resolved into 6 slices from the apex (a) to the base (b), with slice thickness x

The volume was calculated by summing all the areas for a certain phase using the relation:

$$V = x\sum_{i=1}^{n} A_i \quad . \tag{4.7}$$

Where A_i is the area of slice i and x is the slice thickness.

(b) Results and Discussion

Figure 4.3 illustrated the difference between diabetic and healthy groups at the end-diastole and end-systole areas for mid-ventricle slice. The LV end-diastolic volume was taken as the largest cardiac cycle volume (phase 1) and the LV end-systolic volume was taken as the lowest cardiac cycle volume (phase 6). There was a significant decrease ($P<0.001$) in the LV end-diastolic volume in the diabetic rats; the end-systolic volume, however, showed a significant increase ($P<0.01$) in diabetic rats when compared with healthy (Fig.4.4).

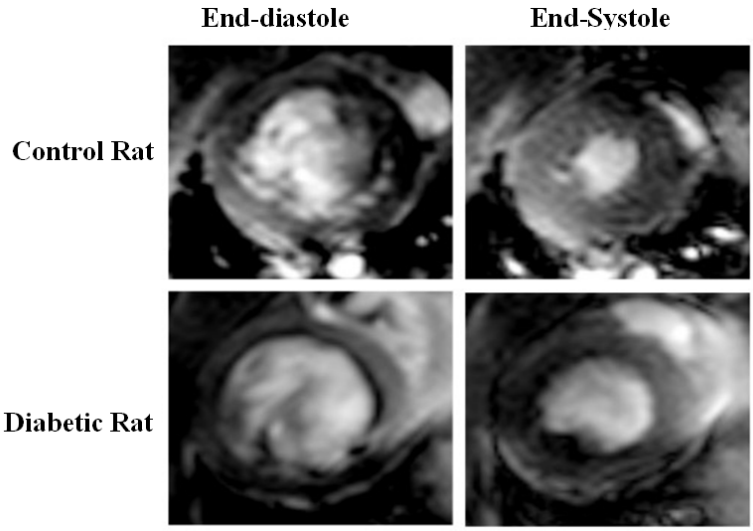

Figure 4.3: Short axis LV at end-diastole and at end-systole for healthy and diabetic animal

Stroke volume and ejection fraction were significantly decreased (P< 0.01) in diabetic rats when compared with healthy. Moreover, the flow volume velocity (dV/dt), also, showed a significant decrease in diabetic group except at the end-systolic phase (Fig. 4.5). In this study we utilized ECG gating to correlate the image acquisition with electromechanical end diastole to obtain functional information on the diabetic LV. The use of cine MRI to image the LV along the cardiac short axis

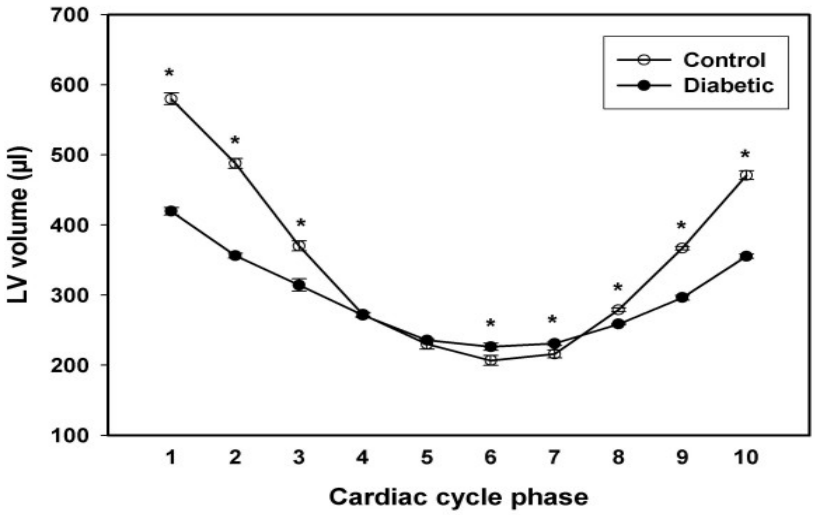

Figure 4.4: LV volume changes during one cardiac cycle between the healthy and the diabetic groups (* means the difference is significant).

provided excellent temporal resolution to delineate volume changes. The high contrast between the blood and endocardium allowed us to perform the planimetry on LV cavities from all images representing the ten phases of cardiac cycle. LV volume calculations showed a significant reduction of 28% in the mean end-diastolic volume of the diabetic group compared to healthys. It has been suggested that the reduction of end-diastolic volume might be the undesirable consequence of an

adaptive mechanism of stiff myocardium, in an effort to compensate for poor contractility by increased pressure during experimental cardiomyopathy [39].

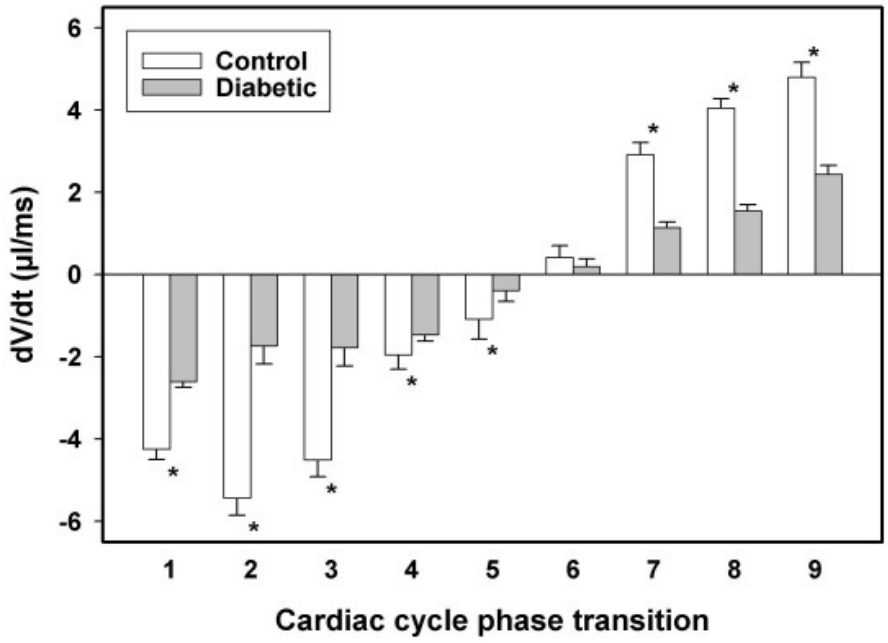

Figure 4.5: The flow velocity changes during one cycle between the two groups (* means significant).

4.3 Exercise Training Improves Cardiac Performance In Diabetes: In Vivo Demonstration With Quantitative Ciné-MRI Analyses

Exercise has long been used as an effective cardio-protective agent in diabetes [40-42]. The structural and functional abnormalities of the diabetic heart respond favorably to exercise training. Endurance training increases the cardiac output in diabetic rats under high-preload conditions [43]. Training prevents the cardiac autonomic nervous dysfunction in diabetes [44] and improves cardiac function in diabetes without benefiting plasma glucose and cholesterol levels [45]. Although these results suggest a favorable role for exercise training on the diabetic heart, the

exercise-induced benefits on cardiac cycle events are not apparent from earlier in vitro or invasive in vivo studies. The importance of obtaining information on the effects of exercise training on the diabetic cardiac cycle events is underscored by the evidence that DCM is associated with both diastolic and systolic left ventricular (LV) dysfunction, resulting in abnormalities of cardiac cycle events [20,46]. Thus the primary objective of this study was to characterize the effects of exercise training on the profound cardiac dysfunction noted in the catabolic state of untreated insulin dependent diabetes. To overcome the interpretive limitations inherent to in vitro and invasive in vivo procedures and study the cardiac cycle events under the relevant biomechanical constraints of the highly dynamic chest cavity, we utilized high-resolution magnetic resonance imaging (MRI) for the evaluation of exercise-induced effects on the diabetic heart. The use of MRI in our investigation was further motivated by the following advantages: 1) the confounding effects of thoracotomy and deep anesthesia that often accompany an invasive approach can be avoided [40]; 2) MRI can capture the cardiac pump function in small animals despite their intrinsically high heart rates [35]; and 3) being intrinsically three-dimensional, MRI computations overcome the limitations posed by geometric assumptions that facilitate volumetric measurements in other commonly used noninvasive procedures, for example, echocardiography [47]. In addition to these unique advantages, the versatility of use and accuracy of measurements made possible by MRI make it ideally suited for cardiac volumetric measurements in heart failure [48]. MRI has also been proposed as the technique of choice for the assessment of treatment effects in

clinical studies due to its accuracy, low inter-observer variability, and the potential to reduce sample size substantially [49].

(a) Procedures and MRI Protocols

In this study, 12 rats were divided equally into three groups to assess the effects of endurance training on the left ventricle cardiac cycle events in diabetes: sedentary control (SC), sedentary diabetic (SD), and exercised diabetic (ED).

Exercise training protocol is discussed in detail in [50]. In summary, the ED group was trained before diabetes induction for 2 weeks; this was followed by 9 weeks of exercise with diabetes. Training speed was increased gradually from 15m/min for 5 min at day one to 20m/min for 50 min at the end of week 2. After diabetes induction, the speed was kept constant at 20m/min for 60 min a day for 9 weeks. After 9 weeks of exercise training, non-invasive cardiac functional evaluation was performed by using high resolution MRI (9.4 T). The same MRI settings for the first paper were used except that we used a higher resolution image matrix with 256x256 pixels. An ECG gated ciné imaging protocol was used to capture the LV cardiac cycle events through 10 equally incremented phases. The results of glucometry at 9-wk diabetes duration are summarized in Table 4.1

(b) Results and Discussion

The main findings of this study were that the cardiac cycle phase volumetric profiles showed favorable functional changes in the ED group (Fig. 4.6),including prevention of decreased end-diastolic volume and attenuation of increased end-systolic

volume that accompanies sedentary diabetes (Fig. 4.7) .

Table 4.1: Glucometry and gravimetry

Rat Group	Plasma Glucose, mg/dl	Hemoglobin A1c,%	Body Mass g	Heart-to-Body Mass Ratio, mg/g
Sedentary control	117±5*	4.8±0.3*	434±12*	3.03±0.16*
Sedentary diabetic	557±18‡	13‡	265±20‡	3.79±0.17‡
Exercised diabetic	569±30‡	11.5±1.0‡	272±28‡	3.82±0.11‡

Values are means SE. *Significantly different from sedentary diabetic group, 0.05. †Significantly different from exercised diabetic group, P<0.05. ‡Significantly different from sedentary control group, P<0.05.

Table 4.2 shows body mass-normalized values of LV volume characteristics for the three groups. There was a 35% decrease in mean LV end-diastolic volume in the SD group compared with the SC group. Exercise training prevented this decrease in diabetes to a considerable extent with only 6% decrease compared with the non-diabetic sedentary lifestyle (Fig. 4.8 a). In addition to the decrease in end diastolic

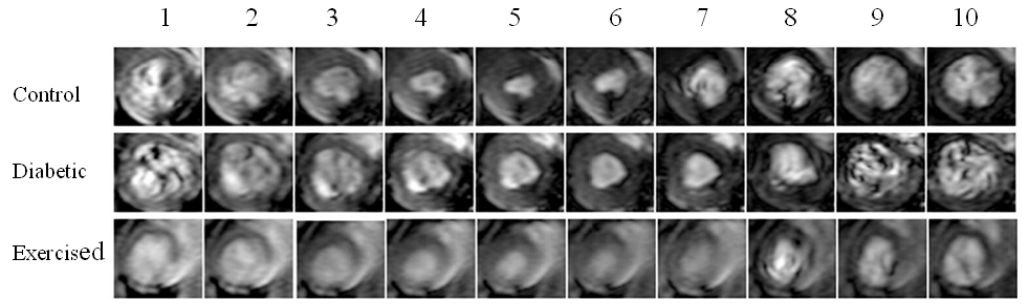

Figure 4.6: Short axis Cardiac cycle phase images for the three groups (end diastolic at phase 1 and end systolic at phase 6 in all three groups)

volume, the LV end- systolic volume was increased by 8% in the SD group compared with the SC group.

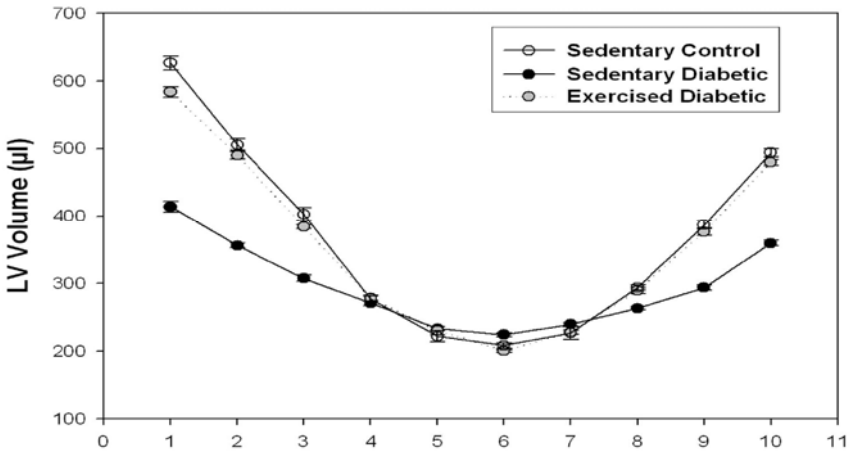

Figure 4.7: Cardiac cycle phase volumetric profiles from the SC, SD, and ED groups. Values are means±SE

Table 4.2: Body mass-normalized values of LV volume characteristics

Parameter	Sedentary control	Sedentary Diabetic	Exercised Diabetic
Myocardial volume, mm3 /g	1.14±0.12*†	2.06±0.30‡	2.05±0.10‡
End-diastolic volume, µl/g	1.49±0.06†	1.59±0.15†	2.19±0.17*‡
End-systolic volume, µl/g	0.48±0.01*†	0.86±0.06‡	0.75±0.05‡
Stroke Volume, µl/g	0.97±0.05†	0.73±0.09†	1.44±0.12*‡
LV output, µl.min-1.g-1	0.28±0.02	0.21±0.02†	0.37±0.03*

Values are means ± SE. LV, left ventricular. *Significantly different from sedentary diabetic group; $P < 0.05$. †Significantly different from exercised diabetic group, $P < 0.05$. ‡Significantly different from sedentary control group, $P < 0.05$.

Meanwhile, the end-systolic volume in the ED group was decreased by 4% compared with the SC group (Fig. 4.8).Accordingly the LV stroke volume and ejection fraction were decreased (55 and 32%, respectively) in the SD group with a decrease (of 8 and

2%, respectively) in the ED compared with the SC group (Fig. 4.8 c and *d*, respectively). The LV output decreased by 58% in the SD group and 25% in the ED group compared with the SC group, indicating that exercise training was able to prevent the decline in LV output that accompanies a sedentary lifestyle in diabetes (Fig. 4.8 e). It should be noted that the difference between groups in the LV output was the results of differences in the stroke volume because the heart rate was not different between groups as mentioned earlier.

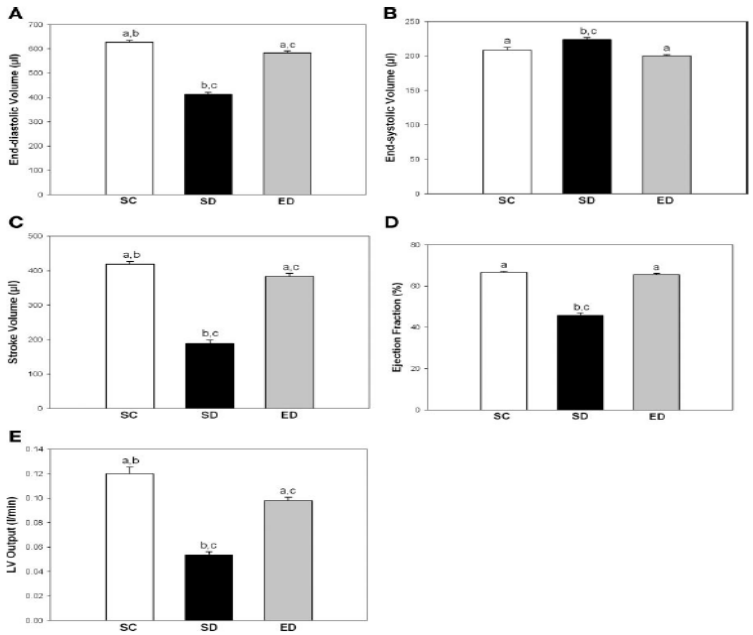

Figure 4.8: Volumetric indexes of cardiac cycle events from SC, SD, and ED animals. LV end-diastolic (*A*) and end-systolic (*B*) volumes of all 3 groups were obtained directly from the phase volumetric profiles in Fig. 4.7 Derived indexes, i.e., LV stroke volume (*C*), LV ejection fraction (*D*), and LV output (*E*) were indicative of cardiac performance differences between groups. Values are means ± SE.

The defects in LV systolic flow velocity, acceleration, and jerk (time derivative of acceleration) associated with sedentary diabetes were restored toward healthy levels in the trained diabetic animals (Fig. 4.9). This MRI study confirms the

prevailing evidence from earlier in vitro and in vivo invasive procedures that exercise training benefits cardiac function in this model of diabetic cardiomyopathy despite the extreme catabolic state of the animals.

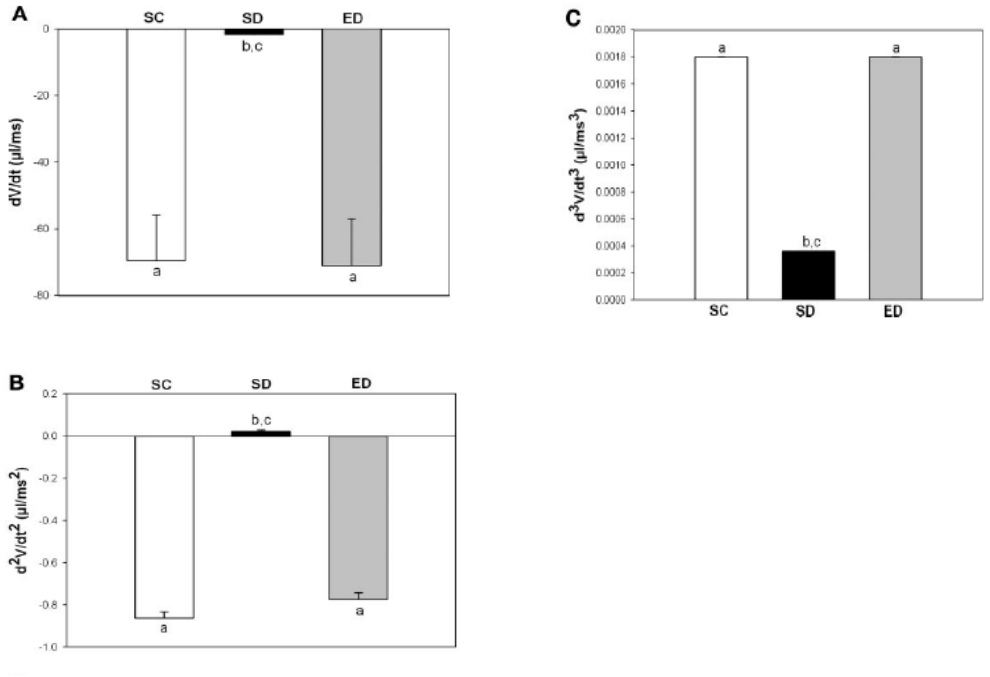

Figure 4.9: LV systolic hemodynamic indexes from SC, SD, and ED animals. LV systolic hemodynamic measures were estimated from the derivatives of the third-order polynomial fit of the cardiac cycle systolic phase volume components (phases 1-6). Values are means ± SE of the instantaneous rates of change that correspond to the phase domains within the systole.

In summary, this is the first MRI evaluation, to our knowledge, of exercise-induced benefits on the diabetic heart and demonstrates that moderate-endurance training, in addition to attenuating cardiac structural defects [50], also improves cardiac cycle volume and hemodynamic profiles. Interestingly, the functional benefits on the diabetic heart occurred in the absence of plasma glucose control or significant benefits on the body mass of the diabetic animals, confirming the results obtained

previously via invasive approaches [45, 51-53]. Taken together, these physiological results nevertheless suggest the possibility of locally occurring molecular correlations of training-induced benefits on cardiac pump function independent of systemic glucose homeostasis in diabetes mellitus. The benefits of training on the efficacy of diabetic cardiac function derived from the use of various animal models, however, are not without translational limitations to human Type 1 diabetes. The major limitation of this study is the acute diabetic state, including the extreme catabolic state of the animals accompanied by permanent hyperglycemia and loss of body mass, which does not represent the current clinical course of long-term diabetes that elicits impaired myocardial function. Hence, future experiments will require studies in hyperglycemic animals that have reasonable maintenance of body mass to provide a valid model to address cellular and molecular mechanisms of DCM. This study was, however, able to demonstrate the tremendous beneficial effects of exercise, despite the catabolic state of the rats, and further verified MRI as a promising tool for the noninvasive evaluation of cardiac function.

References

1. Frangi, A. F., W. J. Niessen, and M. A. Viergever, *Three-dimensional modeling for functional analysis of cardiac images: a review.* IEEE Trans Med Imaging, 2001. **20**: p. 2-25.
2. Hashim, S. and D. Richens, *Finite element method in cardiac surgery.* Interact Cardiovasc Thorac Surg, 2006. **5**: p. 5-8.
3. Tanki, N., K. Murase, M. Kumashiro, R. Momoi, X. Yang, T. Tabuchi, M. Nagayama, and Y. Watanabe, *Quantification of left ventricular volumes from cardiac cine MRI using active contour model combined with gradient vector flow.* Magn Reson Med Sci, 2005. **4**: p. 191-6.
4. Ozturk, C. and E. R. McVeigh, *Four-dimensional B-spline based motion analysis of tagged MR images: introduction and in vivo validation.* Phys Med Biol, 2000. **45**: p. 1683-702.
5. O'Dell, W. G., C. C. Moore, W. C. Hunter, E. A. Zerhouni, and E. R. McVeigh, *Three-dimensional myocardial deformations: calculation with displacement field fitting to tagged MR images.* Radiology, 1995. **195**: p. 829-35.
6. Luo, G. and P. A. Heng, *LV shape and motion: B-spline-based deformable model and sequential motion decomposition.* IEEE Trans Inf Technol Biomed, 2005. **9**: p. 430-46.
7. Osman, N. F., E. R. McVeigh, and J. L. Prince, *Imaging heart motion using harmonic phase MRI.* IEEE Trans Med Imaging, 2000. **19**: p. 186-202.

8. Alrefae, T., I. V. Smirnova, L. T. Cook, and M. Bilgen, *A model-based time-reversal of left ventricular motion improves cardiac motion analysis using tagged MRI data.* Biomed Eng Online, 2008. **7**: p. 15.

9. Specht, Karsten, *The general scope.* e book, 2003: p. 13-15.

10. Fuchs, T. O., M. Kachelriess, and W. A. Kalender, *System performance of multislice spiral computed tomography.* IEEE Eng Med Biol Mag, 2000. **19**: p. 63-70.

11. Urasawa, K., S. Kakinoki, I. Sakuma, K. Kanamori, S. Sakamoto, and H. Yasuda, *[Analysis of ventricular wall motion using multislice ECG-gated cardiac X-ray CT: application of the three-dimensional reconstruction technique]*. J Cardiogr, 1986. **16**: p. 19-32.

12. Carr JJ, Danitschek JA, Goff DC, Crouse JR, 3rd, D'Agostino R, Chen MY, Burke GL, *Coronary artery calcium quantification with retrospectively gated helical CT: protocols and techniques.* Int J Cardiovasc Imaging, 2001. **17**: p. 213-220.

13. Bae KT, Hong C, Whiting BR, *Radiation dose in multidetector row computed tomography cardiac imaging.* J Magn Reson Imaging 2004. **19**: p. 859-863.

14. Choi HS, Choi BW, Choe KO, Choi D, Yoo KJ, Kim MI, Kim J, *Pitfalls, artifacts, and remedies in multi- detector row CT coronary angiography.* Radiographics 2004. **24**: p. 787-800.

15. Hasuda T, Satoh T, Yamada N, Sakamaki F, Kyotani S, Nakanishi N, Kosakai Y, *A case of constrictive pericarditis with local thickening of the pericardium*

without manifest ventricular interdependence. Cardiology 1999. **92**: p. 214-216.

16. Zerhouni, E. A., D. M. Parish, W. J. Rogers, A. Yang, and E. P. Shapiro, *Human heart: tagging with MR imaging--a method for noninvasive assessment of myocardial motion.* Radiology, 1988. **169**: p. 59-63.

17. Axel, L. and L. Dougherty, *MR imaging of motion with spatial modulation of magnetization.* Radiology, 1989. **171**: p. 841-5.

18. Sampath, Smita, *Magnetic Resonance Pulse Sequences for Rapid Imaging of Myocardial Motion and Strain.* PhD dissertation, 2004.

19. Akagawa, E., K. Murata, N. Tanaka, H. Yamada, T. Miura, H. Kunichika, Y. Wada, Y. Hadano, T. Tanaka, Y. Nose, K. Yasumoto, M. Kono, and M. Matsuzaki, *Augmentation of left ventricular apical endocardial rotation with inotropic stimulation contributes to increased left ventricular torsion and radial strain in normal subjects: quantitative assessment utilizing a novel automated tissue tracking technique.* Circ J, 2007. **71**: p. 661-8.

20. Loganathan, R., M. Bilgen, B. Al-Hafez, M. D. Alenezy, and I. V. Smirnova, *Cardiac dysfunction in the diabetic rat: quantitative evaluation using high resolution magnetic resonance imaging.* Cardiovasc Diabetol, 2006. **5**: p. 7.

21. Loganathan, R., M. Bilgen, B. Al-Hafez, S. V. Zhero, M. D. Alenezy, and I. V. Smirnova, *Exercise training improves cardiac performance in diabetes: in vivo demonstration with quantitative cine-MRI analyses.* J Appl Physiol, 2007. **102**: p. 665-72.

22. Ingels, N. B., Jr., G. T. Daughters, 2nd, E. B. Stinson, and E. L. Alderman, *Measurement of midwall myocardial dynamics in intact man by radiography of surgically implanted markers.* Circulation, 1975. **52**: p. 859-67.

23. Henson, R. E., S. K. Song, J. S. Pastorek, J. J. Ackerman, and C. H. Lorenz, *Left ventricular torsion is equal in mice and humans.* Am J Physiol Heart Circ Physiol, 2000. **278**: p. H1117-23.

24. Petitjean, C., N. Rougon, and P. Cluzel, *Assessment of myocardial function: a review of quantification methods and results using tagged MRI.* J Cardiovasc Magn Reson, 2005. **7**: p. 501-16.

25. Bower, A.F., *Applied Mechanics of Solids.* 2009.

26. Fang, Z. Y., J. B. Prins, and T. H. Marwick, *Diabetic cardiomyopathy: evidence, mechanisms, and therapeutic implications.* Endocr Rev, 2004. **25**: p. 543-67.

27. Beache, G. M., V. J. Wedeen, R. M. Weisskoff, P. T. O'Gara, B. P. Poncelet, D. A. Chesler, T. J. Brady, B. R. Rosen, and R. E. Dinsmore, *Intramural mechanics in hypertrophic cardiomyopathy: functional mapping with strain-rate MR imaging.* Radiology, 1995. **197**: p. 117-24.

28. Galderisi, M., K. M. Anderson, P. W. Wilson, and D. Levy, *Echocardiographic evidence for the existence of a distinct diabetic cardiomyopathy (the Framingham Heart Study).* Am J Cardiol, 1991. **68**: p. 85-9.

29. Mandinov, L., F. R. Eberli, C. Seiler, and O. M. Hess, *Diastolic heart failure.* Cardiovasc Res, 2000. **45**: p. 813-25.

30. Xia, L., M. Huo, Q. Wei, F. Liu, and S. Crozier, *Analysis of cardiac ventricular wall motion based on a three-dimensional electromechanical biventricular model.* Phys Med Biol, 2005. **50**: p. 1901-17.

31. Poirier, P., P. Bogaty, C. Garneau, L. Marois, and J. G. Dumesnil, *Diastolic dysfunction in normotensive men with well-controlled type 2 diabetes: importance of maneuvers in echocardiographic screening for preclinical diabetic cardiomyopathy.* Diabetes Care, 2001. **24**: p. 5-10.

32. Tziakas, D. N., G. K. Chalikias, and J. C. Kaski, *Epidemiology of the diabetic heart.* Coron Artery Dis, 2005. **16 Suppl 1**: p. S3-S10.

33. Hayat, S. A., B. Patel, R. S. Khattar, and R. A. Malik, *Diabetic cardiomyopathy: mechanisms, diagnosis and treatment.* Clin Sci (Lond), 2004. **107**: p. 539-57.

34. Fein, F. S. and E. H. Sonnenblick, *Diabetic cardiomyopathy.* Prog Cardiovasc Dis, 1985. **27**: p. 255-70.

35. Vallee, J. P., M. K. Ivancevic, D. Nguyen, D. R. Morel, and M. Jaconi, *Current status of cardiac MRI in small animals.* Magma, 2004. **17**: p. 149-56.

36. van den Bosch AE, Robbers-Visser D, Krenning BJ, McGhie JS, Helbing and Meijboom FJ WA, Roos-Hesselink JW, *Comparison of real-timethree-dimensional echocardiography to magnetic resonanceimaging for assessment of left ventricular mass.* Am J Cardiol, 2006. **97**: p. 113-117.

37. Qin, J. X., M. Jones, A. Travaglini, J. M. Song, J. Li, R. D. White, H. Tsujino, N. L. Greenberg, A. D. Zetts, J. A. Panza, J. D. Thomas, and T. Shiota, *The accuracy of left ventricular mass determined by real-time three-dimensional echocardiography in chronic animal and clinical studies: a comparison with postmortem examination and magnetic resonance imaging.* J Am Soc Echocardiogr, 2005. **18**: p. 1037-43.

38. *Image J.* http://rsb.inf.nih.gov/ij/.

39. Kapelko, V. I., V. I. Veksler, M. I. Popovich, and R. Ventura-Clapier, *Energy-linked functional alterations in experimental cardiomyopathies.* Am J Physiol, 1991. **261**: p. 39-44.

40. Paulson, D. J., S. J. Kopp, D. G. Peace, and J. P. Tow, *Myocardial adaptation to endurance exercise training in diabetic rats.* Am J Physiol, 1987. **252**: p. R1073-81.

41. Monteiro P, Goncalves L, Providencia LA, *Diabetes and cardiovasculardisease: the road to cardioprotection.* Heart, 2005. **91**: p. 1621-1625.

42. Lehmann, R., V. Kaplan, R. Bingisser, K. E. Bloch, and G. A. Spinas, *Impact of physical activity on cardiovascular risk factors in IDDM.* Diabetes Care, 1997. **20**: p. 1603-11.

43. DeBlieux PM, Barbee RW, McDonough KH, Shepherd RE, *Exercise training improves cardiac performance in diabetic rats.* Proc Soc Exp BiolMed, 1993. **203**: p. 209-213.

44. De Angelis KL, Oliveira AR, Dall'Ago P, Peixoto LR, Gadonski G, and Fernandes TG Lacchini S, Irigoyen MC, *Effects of exercise training on autonomic and myocardial dysfunction in streptozotocin-diabetic rats.* Braz J Med Biol Res 2000. **33**: p. 635-641.

45. Korte, F. S., E. A. Mokelke, M. Sturek, and K. S. McDonald, *Exercise improves impaired ventricular function and alterations of cardiac myofibrillar proteins in diabetic dyslipidemic pigs.* J Appl Physiol, 2005. **98**: p. 461-7.

46. Al-Shafei, A. I., R. G. Wise, G. A. Gresham, T. A. Carpenter, L. D. Hall, and C. L. Huang, *Magnetic resonance imaging analysis of cardiac cycle events in diabetic rats: the effect of angiotensin-converting enzyme inhibition.* J Physiol, 2002. **538**: p. 555-72.

47. Heatlie, G. J. and K. Pointon, *Cardiac magnetic resonance imaging.* Postgrad Med J, 2004. **80**: p. 19-22.

48. Narayan, G., K. Nayak, J. Pauly, and B. Hu, *Single-breathhold, four-dimensional, quantitative assessment of LV and RV function using triggered, real-time, steady-state free precession MRI in heart failure patients.* J Magn Reson Imaging, 2005. **22**: p. 59-66.

49. Bellenger, N. G., L. C. Davies, J. M. Francis, A. J. Coats, and D. J. Pennell, *Reduction in sample size for studies of remodeling in heart failure by the use of cardiovascular magnetic resonance.* J Cardiovasc Magn Reson, 2000. **2**: p. 271-8.

50. Searls YM, Smirnova IV, Fegley BR, Stehno-Bittel L., *Exercise attenuates diabetes-induced ultrastructural changes in rat cardiac tissue.* Med Sci Sports Exerc, 2004. **36**: p. 1863-1870.

51. Broderick, T. L., R. St-Laurent, S. Rousseau-Migneron, G. Tancrede, and A. Nadeau, *Beneficial effect of exercise training on cardiac long-chain acylcarnitine levels in diabetic rats.* Diabetes Res, 1990. **14**: p. 83-6.

52. Paulson, D. J., R. Mathews, J. Bowman, and J. Zhao, *Metabolic effects of treadmill exercise training on the diabetic heart.* J Appl Physiol, 1992. **73**: p. 265-71.

53. Villanueva, D. S., P. Poirier, P. R. Standley, and T. L. Broderick, *Prevention of ischemic heart failure by exercise in spontaneously diabetic BB Wor rats subjected to insulin withdrawal.* Metabolism, 2003. **52**: p. 791-7.